Licentiate Thesis in Physics

Core-collapse Supernovae: Theory vs. Observations

Dennis Alp

Particle and Astroparticle Physics, Department of Physics,
KTH Royal Institute of Technology, SE-106 91 Stockholm, Sweden

Stockholm, Sweden 2019

Cover illustration: Two-dimensional projection of the paths of 4096 Monte Carlo photons that escape the supernova ejecta in a simulation of the propagation of the radiation that originates from the radioactive decay of ^{56}Co in the B15 model (Paper III). The post-explosion time of the simulation ranges from 160 to 210 days. During this time, most of the photons are absorbed (not shown), which is the reason for the lack of photons in the central region. The asymmetry of the ejecta is clearly seen by the irregular distribution of escaping photons. The emission is dominated by a region on the left side where the initial radioactive ^{56}Ni was expelled with higher velocities. The photons travel in straight paths between the Compton scattering interactions with electrons. The field of view covers ejecta with radial velocities up to slightly beyond 10,000 km s^{-1}. This implies that the majority of the scattering events occur at positions corresponding to radial velocities of around 3000 km s^{-1}.

Akademisk avhandling som med tillstånd av Kungliga Tekniska högskolan i Stockholm framlägges till offentlig granskning för avläggande av teknologie licentiatexamen torsdagen den 14 februari 2019 kl 15:00 i sal FB52, AlbaNova Universitetscentrum, Roslagstullsbacken 21, Stockholm.

Avhandlingen försvaras på engelska.

ISBN 978-91-7873-062-9
TRITA-SCI-FOU 2019:01

Printed by Universitetsservice US-AB

Till mina föräldrar

Abstract

A core-collapse supernova (CCSN) is an astronomical explosion that indicates the death of a massive star. The iron core of the star collapses into either a neutron star or a black hole while the rest of the material is expelled at high velocities. Supernovae (SNe) are important for the chemical evolution of the Universe because a large fraction of the heavier elements such as oxygen, silicon, and iron are liberated by CCSN explosions. Another important role of SNe is that the ejected material seed the next generation of stars and planets. From observations, it is clear that a large fraction of all massive stars undergo SN explosions, but describing how SNe explode has remained a challenge for many decades.

The attached papers focus on comparing theoretical predictions with observations, primarily observations of SN 1987A. The compact remnant in SN 1987A has not yet been detected and we have investigated how a compact object can remain hidden in the ejecta (Paper I and II). Because of the high opacity of the metal-rich ejecta, the direct X-ray observations are not very constraining even for potentially favorable viewing angles. However, the combined observations still strongly constrain fallback accretion and put a limit on possible pulsar wind activity. The thermal surface emission from a neutron star is consistent with the observations if our line of sight is dust obscured, and only marginally consistent otherwise. Future observations provide promising opportunities for detecting the compact object.

We have also compared the most recent three-dimensional neutrino-driven SN models that are based on explosion simulations with early X-ray and gamma-ray observations of SN 1987A (Paper III). The models that are designed to match SN 1987A fit the data well, but not all tensions can be explained by choosing a suitable viewing angle. More generally, the asymmetries do not affect the early emission qualitatively and different progenitors of the same class result in similar early emission. We also find that the progenitor metallicity is important for the low-energy X-ray cutoff. Current instruments should be able to detect this emission from SNe at distances of 3–10 Mpc, which correspond to distances slightly beyond the Local Group.

Sammanfattning

En kärnkollapssupernova (CCSN) är en astronomisk explosion som indikerar slutet av en massiv stjärnas liv. Stjärnans järnkärna kollapsar antingen till en neutronstjärna eller ett svart hål medan resten av materialet slungas iväg med höga hastigheter. Supernovor (SNe) är viktiga för Universums kemiska utveckling eftersom en stor andel av alla tyngre element såsom syre, kisel, och järn frigörs i CCSN-explosioner. Ytterligare en viktig roll för SNe är att nästa generations stjärnor och planeter bildas av det utkastade materialet. Från observationer är det tydligt att en stor andel av alla massiva stjärnor genomgår SN-explosioner, men att förklara hur SNe exploderar har kvarstått som en utmaning under flera decennier.

De bifogade artiklarna fokuserar på att jämföra teoretiska förutsägelser med observationer, primärt observationer av SN 1987A. Det kompakta objektet i SN 1987A har ännu inte blivit detekterat och vi har undersökt hur ett kompakt objekt can förbli dolt i ejektat (Paper I och II). De direkta röntgenobservationerna är inte så begränsande även längs potentiellt gynsamma siktlinjer på grund av det metallrika ejektats höga opacitet. Däremot begränsar kombinationen av alla observationer starkt ackretion och sätter en gräns för möjlig pulsarvindsaktivitet. Den termiska ytstrålningen från en neutronstjärna är konsistent med observationerna om vår siktlinje är skymd av stoft, och bara marginellt konsistent annars. Framtida observationer utgör lovande möjligheter för att detektera det kompakta objektet.

Vi har också jämfört de senaste tredimensionella neutrinodrivna SN-modellerna, som är baserade på explosionssimuleringar, med tidiga röntgen- och gamma-observationer av SN 1987A (Paper III). SN 1987A-modellerna passar datan väl, men alla diskrepanser kan inte förklaras av ett lämpligt val av observationsvinkel. Generellt så påverkar inte asymmetrierna den tidiga emissionen kvalitativt och olika föregångarstjärnor av samma kategori resulterar i likartad strålning. Vi finner också att föregångarstjärnans metallisitet är viktig för egenskaperna av lågenergiröntgenstrålningen. Befintliga instrument borde kunna detektera denna emission på 3–10 Mpc, vilket motsvarar avstånd lite bortom den Lokala galaxhopen.

List of Publications

Publications Included in the Thesis

Paper I

The 30 Year Search for the Compact Object in SN 1987A
Alp, Dennis; Larsson, Josefin; Fransson, Claes; Indebetouw, Remy; Jerkstrand, Anders; Ahola, Antero; Burrows, David; Challis, Peter; Cigan, Phil; Cikota, Aleksandar; Kirshner, Robert P.; van Loon, Jacco Th.; Mattila, Seppo; Ng, C.-Y.; Park, Sangwook; Spyromilio, Jason; Woosley, Stan; Baes, Maarten; Bouchet, Patrice; Chevalier, Roger; Frank, Kari A.; Gaensler, B. M.; Gomez, Haley; Janka, Hans-Thomas; Leibundgut, Bruno; Lundqvist, Peter; Marcaide, Jon; Matsuura, Mikako; Sollerman, Jesper; Sonneborn, George; Staveley-Smith, Lister; Zanardo, Giovanna; Gabler, Michael; Taddia, Francesco; Wheeler, J. Craig
The Astrophysical Journal, Volume 864, Issue 2, article id. 174, 24 pp. (2018)
DOI: 10.3847/1538-4357/aad739

Author's contribution: The initial outline for this project was conceived by Josefin Larsson. I lead the work and prepared the vast majority of the paper. I wrote the entire manuscript except for Section 2.1 and Appendix A. I generated all the figures and tables except for Figures 9 and 10. The reduced ALMA, VLT, and *HST* data were provided to me by co-authors (though, I repeated the reduction of the *HST* data). A co-author also provided the bootstrapped uncertainties for the position presented in Section 3.1.

Paper II

X-Ray Absorption in Young Core-collapse Supernova Remnants
Alp, Dennis; Larsson, Josefin; Fransson, Claes; Gabler, Michael; Wongwathanarat, Annop; Janka, Hans-Thomas
The Astrophysical Journal, Volume 864, Issue 2, article id. 175, 15 pp.

(2018)
DOI: 10.3847/1538-4357/aad737

Author's contribution: This project accompanies Paper I and includes more general results. I lead the work, wrote all code, and wrote the entire manuscript except for Section 2.4 and parts of Section 2.5 of the paper. I generated all figures and tables, except for Figure 1.

Paper III

Early X-Ray and Gamma-Ray Emission from 3D Neutrino-Driven SN Simulations and Comparisons With Observations of SN 1987A
Alp, Dennis; Larsson, Josefin; Fransson, Claes; Maeda, Keiichi; Gabler, Michael; Wongwathanarat, Annop; Janka, Hans-Thomas; Jerkstrand, Anders
Manuscript soon to be submitted to The Astrophysical Journal

Author's contribution: The initial outline for this project was conceived by Claes Fransson. I lead the work and wrote most of the code used for the simulations. I wrote the entire manuscript except for parts of Section 1. I generated all the figures and tables. The simulations related to the W18 and W20 models were performed by Keiichi Maeda.

Contents

Chapter 1

Introduction

Core-collapse supernovae (CCSNe) are the violent deaths of massive stars. They are extremely energetic and can shine as brightly as ten billion Suns. CCSN explosions are only triggered in stars that are at least around ten times more massive than the Sun. The driving mechanism that disrupts the stars is only active for around one second, but supernovae (SNe) trap this energy and shine brightly for several months. The remaining energy is dissipated in the subsequent SN remnant (SNR) phase, which can be slowly fading for thousands of years. Each CCSN explosion creates either a neutron star or a black hole and typically expels several solar masses of material into space at velocities of many thousand kilometers per second.

CCSNe play several important roles in astrophysics. They are important producers of elements from oxygen to iron, crucially affecting the chemical evolution of galaxies and the Universe. Most of the matter that we see around us have once been synthesized inside a star that expelled the material in a SN explosion. The chemically enriched material that is expelled at high velocities and its kinetic energy shape galaxies. These are the processes that seed the next generation of stars and allow new planets to form. The neutron stars and black holes that are created by CCSNe are among the most extreme environments in the Universe. They allow us to test fundamental physics in regimes that are impossible to probe anywhere else.

SNe have been observed by ancient astronomers long before they were understood to be astrophysical explosions. Famous historical examples are the Crab Supernova (SN 1054, Figure 1.1), Tycho's Supernova (SN 1572; Brahe 1573), and Kepler's Supernova (SN 1604; Kepler 1606). The term "supernova" was coined by Baade and Zwicky (1934), where they also "advanced the view that a super-nova represents the transition of an ordinary star into a neutron star". Much of the foundations of how elements are

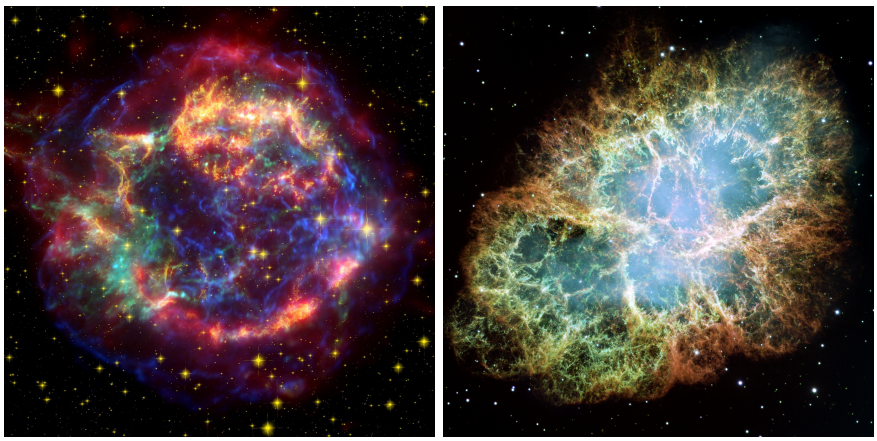

Figure 1.1. The two well-observed SNRs Cas A (left) and the Crab Nebula (right).

Image credits:
Left. NASA/JPL-Caltech, Oliver Krause (Steward Observatory), George H. Rieke (Steward Observatory), Stephan M. Birkmann (Max-Planck-Institut fur Astronomie), Emeric Le Floc'h (Steward Observatory), Karl D. Gordon (Steward Observatory), Eiichi Egami (Steward Observatory), John Bieging (Steward Observatory), John P. Hughes (Rutgers University), Erick Young (Steward Observatory), Joannah L. Hinz (Steward Observatory), Sascha P. Quanz (Max-Planck-Institut fur Astronomie), Dean C. Hines (Space Science Institute), 9 June 2005
Right. NASA, ESA, STScI, J. Hester and A. Loll (Arizona State University), 1 December 2005

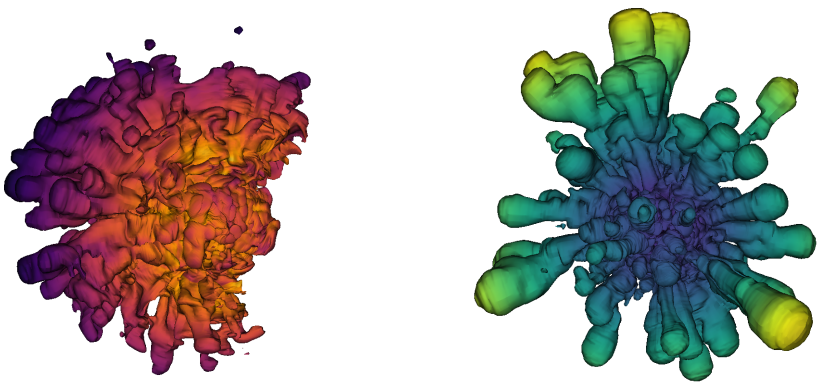

Figure 1.2. Visualizations of 3D SN models based on computer simulations of the neutrino-driven explosion mechanism. The progenitors are a binary merger (left, Menon and Heger, 2017; Menon et al., 2019) and the B15 model (right, Wongwathanarat et al., 2015). The color scales represent the radial velocity.

created in stars and SN explosion were developed during the 1950s (Hoyle, 1954; Burbidge et al., 1957; Hoyle and Fowler, 1960). The first outline of how the liberated gravitational potential energy can be deposited into the envelope and turn a central collapse into an explosion in most SNe was made by Colgate and White (1966), Arnett (1966), and Bethe and Wilson (1985). A particular event of major importance is SN 1987A, which is the closest observed SN in more than four centuries. This has helped advance the field and allowed for observations of unprecedented detail. Another factor that has helped progress the field of CCSNe during the past few decades is the rapid development of computational resources.

The level of this licentiate thesis is set such that it should be accessible to any reader with a background in any field of physics. This implies that parts of the introduction to subfields specific to astrophysics are at a relatively basic level and that important fundamental concepts are reviewed. The experienced reader will hopefully find a couple of interesting notes and alternative perspectives of familiar subjects. Parts of Sections 3.2–3.4 are based on the unpublished reports "An X-ray View of Supernova Remnants" for the course AS7001 and "Explosion Mechanisms of Core-Collapse Supernovae" for the course AS7016 at Stockholm University, which were written by the same author.

1.1 Context

One of the critical questions that remains unanswered is how massive stars explode. This has proven to be particularly difficult to solve because CCSNe are highly complex processes, which involve a number of different physical phenomena. In fact, it is one of the few physical processes where all four fundamental forces are contributing at significant levels. The problem is further complicated by the very large dynamic range of timescales and lengthscales. The evolution of a massive star spans millions of years and the core collapse occurs on timescales of milliseconds. The detailed physics also depend on interactions at a microscopic level in systems that are larger than the Sun. Additionally, CCSNe are clearly 3-dimensional (3D) processes. As a consequence of the multifaceted physics and dynamic ranges, accurate simulations based on first principles have remained computationally unfeasible.

Over the past decades, different theories have evolved to describe different parts of the explosion process. These theories make observable predictions about the properties of the stars just before the explosion, the particles and radiation emitted by the star during the explosion, and what will remain after the bright SN starts to fade. The currently favored explosion mechanism is the delayed neutrino-heating mechanism (for reviews, see Janka, Marek and Kitaura, 2007; Janka, Langanke, Marek, Martínez-Pinedo and

Müller, 2007; Janka, 2012; Burrows, 2013; Müller, 2016; Janka, 2017). At best, it can successfully describe the explosion of the most common SNe. It is clear that a small number of more extreme SNe require additional processes to be active. Another independent uncertainty is the accuracy of the progenitor models. SN simulations are fundamentally initial value problems and cannot be expected to be more accurate than the progenitor models.

The aim of the work in this thesis has been to compare predictions of SN theory with observations. The attached papers investigate observables related to SN progenitors, the explosion mechanism, the formation of compact objects, and possibilities of future observations. These comparisons allow us to test how accurate the current description of CCSNe is. We have focused on comparing predictions of the delayed neutrino-driven mechanism with observations of SN 1987A. There are several properties of the theory that can be tested observationally, such as if a neutron star or black hole remains after the explosion (Paper I), the 3D structure of the ejecta (Paper II and III), and how the material is mixed in the turbulent explosions (Paper III). These comparisons are a small subset of all observational criteria that any successful explosion theory needs to fulfill.

1.2 Conventions

Readers unfamiliar with astronomy might find many unusual units and technical terms. The purpose of this section is to introduce some of the jargon. Astronomers generally use centimeter-gram-second (cgs) units but there are also a number of additional units in different subfields that have been introduced for special purposes. A list of common units is provided in Table 1.1, and physical and astronomical constants in Table 1.2. Optical fluxes are often given in magnitudes. This is a historic measure of observed flux and must be calibrated using a given zeropoint. Without going into the details, the important properties are that each change of 1 mag corresponds to a change in flux of a factor of 2.5 and the magnitude scale is reversed (brighter objects have lower or more negative magnitudes). It is worth emphasizing the distinction between magnitude (mag) and order of magnitude (factors of 10). The unit Crab is sometimes used in X-ray instrumentation and is simply the observed flux of the Crab Nebula (Kirsch et al., 2005). This is complicated by the fact that the observed flux varies depending on the given energy interval. The unit "beam" is mostly used toward longer wavelengths and is a measure of the solid angle subtended by each independent spatial measurement. It is the analogue of a pixel for raster (pixelized) images.

Astronomers also label different intervals of the electromagnetic spectrum roughly following the conventions in Table 1.3. The dividing lines are not strict and could vary slightly depending on context. I note that

Table 1.1. Astronomical Units

Quantity	Unit	Symbol	Equivalent
Length	centimeter	cm	0.01 m
Mass	gram	g	0.001 kg
Time	second	s	1 s
Energy	erg	erg	10^{-7} J
Energy	electronvolt	eV	1.602×10^{-12} erg
Magnetic flux density	Gauss	G	10^{-4} T
Energy	Bethe	B	10^{51} erg
Energy	$10^{\text{fifty-one}}$ ergs	foe	10^{51} erg
Flux density	Jansky	Jy	10^{-23} erg s^{-1} cm^{-2} Hz^{-1}
Length	light year	ly	9.463×10^{17} cm
Length	parsec	pc	3.086×10^{18} cm
Angle	minute of arc (arcminute)	$'$	$(1/60)^\circ$
Angle	second of arc (arcsecond)	$''$	$[1/(60 \times 60)]^\circ$
Angle	milliarcsecond	mas	$[1/(60 \times 60 \times 1000)]^\circ$
Angle	hour angle	$^{\text{h}}$	$(360/24)^\circ$
Angle	minute angle	$^{\text{m}}$	$[360/(24 \times 60)]^\circ$
Angle	second angle	$^{\text{s}}$	$[360/(24 \times 60 \times 60)]^\circ$
Flux	magnitude	mag	...[†]
Flux	Crab	Crab	...[†]
Solid angle	beam	beam	...[†]

[†]See Section 1.2 for details

Table 1.2. Physical and Astronomical Constants

Name	Symbol	Value
Speed of light in vacuum	c	$2.99792458 \times 10^{10}$ cm s^{-1}
Gravitational constant	G	6.67408×10^{-8} cm^3 g^{-1} s^{-2}
Planck constant	h	6.626×10^{-27} erg s^{-1}
Thomson cross section	σ_{T}	6.652×10^{-25} cm
Solar radius	$R_\odot$	6.957×10^{10} cm
Solar mass	$M_\odot$	1.989×10^{33} g
Solar luminosity	$L_\odot$	3.828×10^{33} erg s^{-1}

astrophysicists rarely use the term microwave, unless referring to the Cosmic Microwave Background (CMB). Additionally, micron is sometimes seen instead of μm and the wavenumber (inverse wavelength) can be used on rare occasions, especially in MIR. The definition of optical emission can also sometimes extend to more or less include ultraviolet (UV) and near-infrared (NIR). Visible light is sometimes used to explicitly refer to the visible part of the spectrum. I will use optical for visible light (i.e. excluding UV and NIR) and use UVOIR to refer to UV, optical, and NIR combined.

Several of the bands are also subdivided. One of the most common is the distinction between soft and hard X-rays. The limit between soft and hard depends on context. If the current context is restricted to below 10 keV, soft most likely refers to < 2 keV, whereas soft probably refers to < 10 keV if the context extends to 100 keV. The UV band is sometimes separated into near-UV and extreme-UV (or far-UV) and gamma-rays with (much) higher energies are often called (very-)high-energy gamma-rays. Lastly, wavelengths of atomic and molecular transitions can be given in both vacuum and air. The wavelengths in air are slightly shorter because of the refractive index of air of 1.0003. Lines are often given in Ångstroms, which means that a change of the fourth significant digit can occur. For example, the important oxygen line at 5007 Å can also be reported as 5008 Å.

Astronomers sometimes simplify the periodic table into hydrogen, helium, and metals. These can sometimes be denoted X, Y, and Z, respectively. This means that "metals" will exclusively be used in this meaning of "everything heavier than helium". Heavy metals most likely refers to elements from silicon to around iron.

In the context of SNe and SNRs, it is common to refer to the radial position in terms of velocity. This always implicitly assumes that the ejecta is expanding homologously.

Astrometry and photometry are two common astronomical terms. Photometry means measuring the flux of objects and is mostly used to refer to flux measurements in UVOIR bands. Astrometry means measuring positions in the sky. This may sound simple but defining an accurate coordinate frame is actually rather complicated. The International Celestial Reference Frame (ICRF) is the standard reference frame. The International Astronomical Union (IAU) standard is to include the epoch, which is the moment at which the coordinates are valid. The ICRF is a realization of the International Celestial Reference System (ICRS). The ICRF have coordinates that are fixed in space but there are other frames that require an additional time that defines at which moment in time the frame is defined. This time is called the equinox. For example, the coordinate frame that is derived from the Fifth Fundamental Catalogue (FK5) of stars has the standard equinox J2000 (2000 January 1, noon Terrestrial Time).

Table 1.3. Electromagnetic Spectrum

Name	Frequency	Wavelength	Energy	Common Units
Radio	< 30 GHz	> 10 mm	< 0.1 μeV	MHz, GHz, m, cm
(sub-)mm	30–1000 GHz	10–0.3 mm	0.1–4 μeV	GHz, mm, μm
FIR	1–10 THz	300–30 μm	4–41 μeV	GHz, μm
MIR	10–60 THz	30–5 μm	0.04–0.25 meV	μm
NIR	60–370 THz	5–0.8 μm	0.2–1.5 meV	Å, μm
Optical	370–750 THz	8000–4000 Å	1.5–3.1 meV	nm, Å
UV	$7{\times}10^{14}$–$3{\times}10^{16}$ Hz	4000–100 Å	3–124 meV	nm, Å
X-rays	$3{\times}10^{16}$–$2{\times}10^{22}$ Hz	100 Å–10^{-12} cm	0.1 eV–100 keV	Å, keV
Gamma-rays	$> 2 \times 10^{22}$ Hz	$< 10^{-12}$ cm	> 100 keV	keV, MeV, GeV, TeV

When discussing the distribution of flux over different energy bands, it is common to use the term spectral energy distribution (SED) instead of spectrum. It is also common to multiply the flux density measure (y-axis) by the abscissa (x-axis) quantity in SEDs.

Power laws are often used to describe spectral shapes. Each power law is characterized by a power-law index. This is often called photon index in X-rays and gamma-rays but can be defined in different ways depending on context. The differences are the sign and if it is giving the shape of the photon number flux density or (energy) flux density, which shifts the photon index by 1.

I adopt the view that science describes[1] Nature.

[1]Not explains!

Chapter 2

Supernova Physics

The purpose of this section is to give readers an overview of the most relevant physical processes. The physical processes are typically covered in physics textbooks, but are important enough for this thesis to warrant a qualitative review. More complete descriptions of these subjects can be found in, e.g., Rybicki and Lightman (1979), Cheng (2005), and Harris (2007).

2.1 Emission Processes

This section covers line emission, bremsstrahlung (braking radiation or free-free emission), synchrotron emission, and inverse Compton scattering, which are some of the most common emission processes in astrophysical contexts. Illustrations of the emission processes are provided in Figure 2.1. Electrons are generally more important than positive ions because of the higher charge-to-mass ratio of electrons. Therefore, the processes are typically thought of as electron-dominated but the following principles apply to particles of arbitrary charge.

In astrophysical contexts, line emission (Panel I of Figure 2.1) refers to the emission of photons with characteristic energy. The term "line" refers to the shape of such a spectrum. The photon energy is in most cases determined by differences in energy levels of an atom when an electron transitions from a level of higher energy to a lower energy level. The excess energy is then emitted as a photon. This means that line emission is a discrete emission process, whereas the other processes in this section are continuum processes. However, the energy of these transitions is not always exactly the same. The primary correction to the photon energy is given by the Doppler shift determined by the relative velocity between the source and the observer. Because blue photons are more energetic than red photons, the

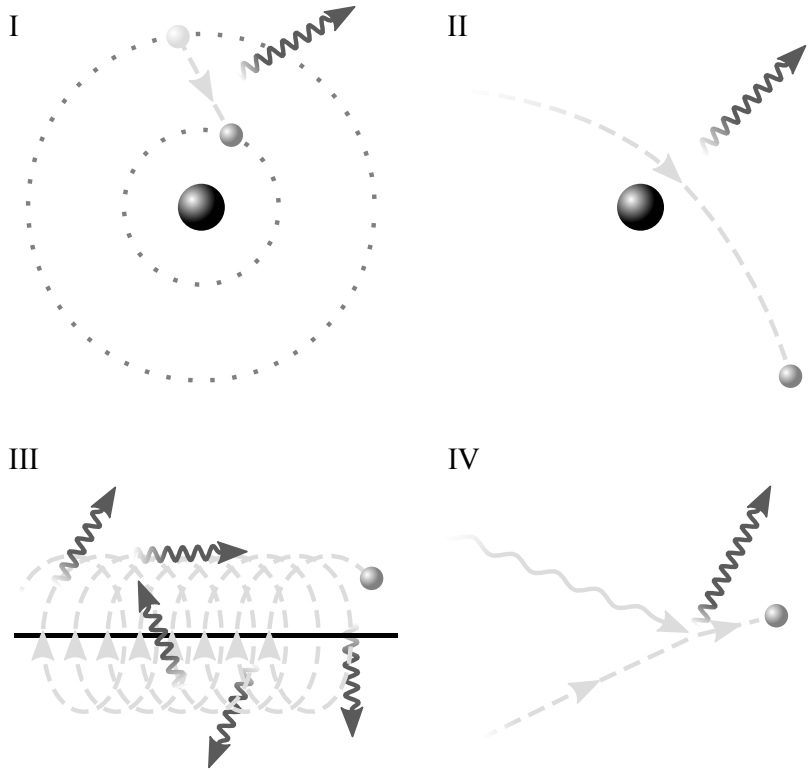

Figure 2.1. Illustrations of four important emission processes. The smaller gray spheres are electrons and the larger black spheres are protons (or any positive nucleus in general). Dashed lines are electron trajectories, the solid black line represents a magnetic field, photons are indicated by waves, and energy levels are illustrated by dotted lines. Line emission (Panel I) occurs when an electron transitions from a higher to a lower energy level in an atom. Bremsstrahlung (or free-free emission, Panel II) is the emission produced by a free electron that is deflected by a positive ion. Synchrotron radiation (Panel III) is produced by a fast electron gyrating in a magnetic field. Inverse Compton scattering (Panel IV) is when a fast electron interacts with a photon and transfers energy from the electron to the photon. See Section 2.1 for details about the emission processes.

terms "blueshift" and "redshift" are often used to denote emission that has been Doppler boosted to higher and lower energies, respectively. It is very common to perform measurements of the Doppler shifts of lines to determine the velocity of an object along the line of sight (radial velocity). Another important property of emission lines is their widths, which are determined by the radial velocity distribution of the individual atoms or macroscopic objects that constitute the source. In most cases, this is dominated by the thermal motion of atoms or the random motions of constituting objects. However, in SNe, the width of the lines are dominated by the bulk motion of the outflow of the material from the center of the explosion. This means that material that is bluer are on the near side, whereas the redder emission originates from the far side. In addition to the energy shift and line width, the line profile is sometimes discussed. The is essentially just analyzing the distribution of the emission at different line-of-sight velocities.

Bremsstrahlung (Panel II of Figure 2.1) involves a fast electron being deflected by a positively charged ion. This is often described in the frame where the ion is stationary and the incoming electron is moving, which is generally a good approximation of the observer's frame because electrons are in general moving much faster than the heavier ions. The acceleration of the electron as it travels through the electric potential leads to the emission of a photon and a corresponding energy decrease of the electron. In typical astrophysical contexts, the emission is characterized by the electron density and energy distribution, as well as the ion density. Notable properties are that the emission depends on the product of the density of the electrons and the ions, and that the photon energy depends on the electron energy.

Synchrotron emission (Panel III of Figure 2.1) is the emission produced by a relativistic electron (see Section 2.3) in the presence of a magnetic field. The acceleration that gives rise to the helical path also gives rise to photons with frequencies proportional to the gyration frequency and speed of the electron. The total power emitted is a function of particle density, the square of the particle energy distribution, and the square of the magnetic field strength. This process is also called cyclotron emission if the particle is non-relativistic.

Inverse Compton scattering (Compton 1923, Panel IV of Figure 2.1) is not strictly an emission process in the sense that photons are created. Instead, inverse Compton is when a high-energy electron interacts with a previously existing low-energy photon and transfers some of the energy from the electron to the photon. This means that any field of low-energy photons could be reprocessed into high-energy photons by high-energy electrons, which is why inverse Compton scattering is often categorized as an emission process. Importantly, the opposite scenario where a high-energy photon imparts energy to a lower-energy electron is also possible. However, this

is often considered an absorption process called Compton scattering (see Section 2.2).

Lastly, it is worth pointing out that blackbody (thermal) emission is not an emission process even though it is often used to describe the emission of a source. Blackbody emission is emission from an opaque, non-reflective source in thermodynamic equilibrium with its environment. Blackbody emission does not specify how the photons are created. A characteristic is that the escaping spectrum is uniquely determined by the temperature of the source. This is because the emitter is opaque and the photons are free to exchange energy with the surroundings, which means that the photons will adopt an energy distribution determined by allowed quantum states that are solely dependent on the temperature (Blundell and Blundell, 2010).

2.2 Absorption Processes

This section covers Compton scattering, photoelectric absorption (photoabsorption), and dust absorption, which are common absorption processes in astrophysical contexts. Illustrations of the emission processes are provided in Figure 2.2. When discussing absorption, it is common to refer to the interaction cross section. This is a measure of how likely the absorption process is and is analogous to the classical cross section of macroscopic objects.

Compton scattering (Panel I of Figure 2.2, see also Paper III) is simply the opposite of inverse Compton scattering (Section 2.1). In the context of this thesis, primarily Compton scattering is of importance because it is the dominating interaction channel for photons with energies in the range 30 keV–3 MeV. Throughout this energy range, the interaction cross section per electron remains relatively constant. This means that (neutral) heavier elements have Compton scattering cross sections that are proportional to the atomic number. Another important property is that Compton scattering does not destroy photons, whereas both photoabsorption and dust absorption do.

Photoelectric absorption (Einstein 1905*a*, Panel II of Figure 2.2, see also Paper II and III) is the process by which a photon is destroyed by an electron that is originally bound to an atom. The electron gets unbound by the incoming energy (which is why photoabsorption is also referred to as bound-free absorption) and the excess energy is converted into kinetic energy of the electron. For SN remnants, photoabsorption is important because it is the dominating absorption channel for photons with energies of 0.01–30 keV. The photoabsorption cross section is very sensitive to both the atomic number of the absorbing atom and the photon energy. The cross

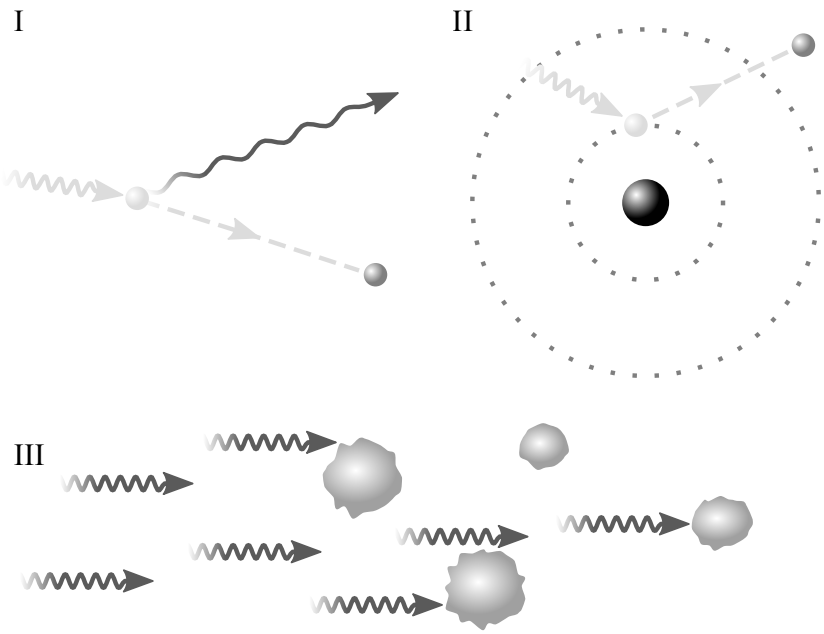

Figure 2.2. Illustrations of three important absorption processes. The smaller gray spheres are electrons and the larger black sphere is a proton (or any positive nucleus in general). Dashed lines are electron trajectories, photons are indicated by waves, energy levels are illustrated by dotted lines, and the irregular gray blobs represent dust. Compton scattering (Panel I) is when a photon scatters off an electron and transfers energy from the photon to the electron. Photoelectric absorption (Panel II) is the process in which a photon is absorbed by an atom and the energy goes into a bound electron, which is liberated by the energy. Dust absorption (Panel III) refers to the absorption of photons by small particles consisting of a large number of atoms. See Section 2.2 for details about the absorption processes.

section steeply increases as the atomic number cubed but quickly drops toward higher energies as the inverse of the energy cubed.

Gas, Molecules, Dust, and Grains

Before outlining properties of dust absorption, it is important to make a distinction between the different components of matter in SN remnants. Gas almost always refers to gas dominated by monoatomic gas, which may or may not be an ionized plasma. If the material consists of molecules such as CO, SiO, H_2, it would most likely be referred to as "molecules", even though it is in a gaseous phase. Grains and dust both refer to small particle solids of a few atoms to a few microns in (linear) size. The compositions of these grains are often uncertain but they are most likely composed of elements that are abundant on Earth in solid compounds, such as carbon, oxygen, silicon, and iron. For intuition, in everyday life, these grains are more likely to be called soot or fine sand.

Dust absorption (Panel III of Figure 2.2) is not strictly a physical absorption process at a microphysical level. However, because dust is ubiquitous in space and the composition is poorly constrained, it is customary to model the dust absorption by a parametrized absorption profile (Cardelli et al., 1989). Dust absorption is most important at UV wavelengths and gradually decreases at longer wavelengths (Draine, 2003).

2.3 Relativity

The purpose of this section is to introduce a number of relativistic effects without going into the theory of relativity. An important prediction of special relativity (Einstein, 1905*b*) is that nothing can move faster than the speed of light in vacuum. The (kinetic) energy of an object can be arbitrarily high, but the velocity will only tend toward the speed of light as the energy goes to infinity. Special relativity also describes the relation

$$E = m\,c^2 \tag{2.1}$$

that relates energy E of an object to its mass m by the speed of light in vacuum c. This is important in a number of astrophysical contexts because some processes are capable of converting a significant fraction of the mass into energy. It is also common to describe particles as relativistic or non-relativistic. This depends on context but is roughly when the (classical) kinetic energy is equal to the $m\,c^2$ energy.

General relativity (Einstein, 1916) only introduces significant corrections to Newtonian gravity (Newton, 1687) in very strong gravitational fields. This only happens in relatively few systems in the Universe. Two examples that are connected to SNe are neutron stars and black holes (see Section 3.5). One consequence of general relativity is that measured quantities are different in different frames and there are two particularly important frames. First, the local frame where quantities are measured at the position of the massive object. These quantities can be denoted local, intrinsic, un-redshifted, or actual. Secondly, the observer's frame "at infinity", which implies far from the deep parts of the gravitational well. These quantities are denoted redshifted, observed, or at infinity. The magnitude of the general relativistic effects are conveniently parametrized by the gravitational redshift parameter (Section 9.3.1 of Becker 2009)

$$g_{\mathrm{r}} = \sqrt{1 - \frac{R_{\mathrm{S}}(M)}{R}}, \tag{2.2}$$

where

$$R_{\mathrm{S}}(M) = \frac{2\,G\,M}{c^2} \tag{2.3}$$

is the Schwarzschild radius, M the mass, R the radius, and G the gravitational constant. For example, $g_{\mathrm{r}} = 0.8$ at the surface for typical neutron star parameters where $g_{\mathrm{r}} = 1$ implies flat spacetime. Let the quantities in the observer's frame be denoted by subscript ∞, then the effects on some common quantities are as follows:

- Length (e.g. radius or photon wavelength) $R_\infty = R/g_{\mathrm{r}}$
- Time (differences) $\Delta t_\infty = \Delta t/g_{\mathrm{r}}$[1]
- Temperature $T_\infty = g_{\mathrm{r}}\,T$
- (Energy) flux $F_\infty = g_{\mathrm{r}}^2\,F$

Additionally, masses are not uniquely defined in some contexts. For neutron stars, it is common to refer to both gravitational and baryonic masses (see Section 5.1 of Zhang et al., 2008). Gravitational mass is the mass that enters into Newton's law of gravity to describe the gravitational potential (at distances not too close to the source). The baryonic mass is the mass that would be measured if you took all particles from the compact object and moved each particle to infinity (very far away from the source) and then measured its mass. For neutron stars, the gravitational and baryonic masses could be different. This is because a substantial fraction of the mass-energy of a neutron star is converted into negative gravitational potential

[1] cf. Interstellar (Nolan, 2014)

energy when the neutron star forms. Imagine a particle falling into a very deep gravitational well. The particle would liberate negative gravitational potential energy and convert it into kinetic energy as it accelerates into the well. In a simplified picture of neutron star formation, this kinetic energy is converted into heat that is subsequently radiated away, which leaves only the negative gravitational potential energy. By the mass-energy equivalence [Equation (2.1)], this means that the sum of the original baryonic mass is higher than the gravitational mass, which is the sum of the baryonic mass (the stuff that actually makes up the star) and the negative gravitational potential energy. For typical neutron star parameters, the ratio of gravitational to baryonic mass is around 0.9 [Equation (36) of Lattimer and Prakash 2001].

Mass Difference and Binding Energy

It is no coincidence that the ratio of gravitational to baryonic mass is similar to the gravitational redshift factor. The Newtonian binding energy for a homogeneous sphere is

$$E_\mathrm{b} = \frac{3\,G\,M^2}{5\,R} \rightarrow M_\mathrm{b} = \frac{3\,G\,M^2}{5\,R\,c^2}, \tag{2.4}$$

where the mass-energy equivalence [Equation (2.1)] was used in the last step and M_b is the mass corresponding to the binding energy. On the other hand, from Equations (2.2) and (2.3), we have that

$$1 - g_\mathrm{r} = 1 - \sqrt{1 - \frac{R_\mathrm{S}(M)}{R}} \approx 1 - \left(1 - \frac{R_\mathrm{S}}{2\,R}\right) = \frac{G\,M^2}{R\,c^2}, \tag{2.5}$$

where the approximation holds for $R_\mathrm{S} \ll R$. From this, it is clear that g_r is approximately the ratio of baryonic to gravitational mass, except for a factor of order unity.

2.4 Nucleosynthesis and Radioactivity

Nucleosynthesis means the combination of nucleons into new nuclei. Stellar nucleosynthesis powers stars, which are stable thermonuclear furnaces throughout their lives (Prialnik, 2000). They are held together by self gravity and the high pressures and temperatures allow for the atoms in the core of the star to undergo fusion. Energy is released by fusing lighter elements into heavier elements up to ^{56}Fe. Energy is liberated by increasing

the (negative) nuclear binding energy. However, combining elements heavier than ^{56}Fe results in a net energy loss because ^{56}Fe has the lowest mass per nucleon[2]. This means that the stable thermonuclear fusion chain starts with hydrogen burning and ends once ^{56}Fe has formed. Explosive or SN nucleosynthesis occurs during the first few seconds after the onset of the explosion (Hix and Harris, 2017). The radioactive elements created during this period are of particular importance because they are the primary power sources for the subsequent phases. When a radioactive element decays, the atomic nucleus loses energy by emitting particles or radiation.

To avoid confusion, I emphasize the difference between half-life (often denoted $T_{1/2}$) and lifetime (often denoted τ). The half-life is the time during which half the original number remains, and lifetime is equivalent to an e-folding time (decreased by a factor of $e \approx 2.71828$). It is also worth noting that, in nuclear physics, helium nuclei are frequently referred to as α particles, electrons as β particles, and positrons as β^+ particles[3]. It is common not to make a distinction between the emission from the decay, and from prompt emission by the daughter nucleus. For example, the astrophysically important lines at 67.87 and 78.39 keV (Grebenev et al., 2012; Grefenstette et al., 2014; Boggs et al., 2015) are often referred to as ^{44}Ti lines, even though they are promptly emitted as a result of nuclear transitions of ^{44}Sc, which is the daughter product of ^{44}Ti. Nuclear transitions implies transitions in the energy levels of nucleons, and not the analogue for electrons, which are more commonly observed. The transition $^{44}\mathrm{Ti} \rightarrow {}^{44}\mathrm{Sc}$ itself is an electron capture transition, which is when $\mathrm{p} + \mathrm{e}^- \rightarrow \mathrm{n} + \nu_\mathrm{e}$.

[2]The isotope ^{62}Ni has the highest binding energy per nucleon (not contradicting because of the difference in proton and neutron mass), which is not formed because it has no prominent formation channel in stars.

[3]This naturally explains the term γ-rays, which is another common product of nuclear reactions.

Chapter 3

Core-collapse Supernovae

There are different types of SNe that are divided into different categories depending on which process that triggers the explosion. This thesis focuses on core-collapse SNe (CCSNe) that are triggered by the collapse of the central iron core. I emphasize the period from just before core collapse to early SNR phase because of its relevance for this thesis.

3.1 Part of a Cosmic Cycle

It is important to highlight that SNe are part of a cosmic cycle that involves the births, evolutions, and deaths of stars. The cycle is completed by the formation of the next generation of stars, which are seeded by the deaths of the previous generation. An arbitrary starting point of the cosmic cycle can be taken to be the interstellar medium (ISM, Draine 2003). For an evolved galaxy, such as the Milky Way, the ISM constitutes approximately 10 % of the baryonic mass (i.e., excluding dark matter). The physics of the ISM is in itself very rich and diverse. One of the most important connections between the ISM and other astrophysical phenomena is star formation.

Exactly how stars form remains one of the open questions in modern astrophysics. The challenge is to describe how the ISM with a mean number density of around 1 cm^{-3} collapses to densities on the order of 10^{26} cm^{-3}, which is the number density in the center of the Sun. The problem consists of overcoming both the gas pressure and magnetic pressure, as well as how the angular momentum is transferred outward.

The next step of the cycle is stellar evolution (Prialnik, 2000). This is more closely connected to SNe because the last stages of stellar evolution determine the initial conditions for CCSNe. Of particular relevance for SNe is the evolution of massive stars. The most basic description of

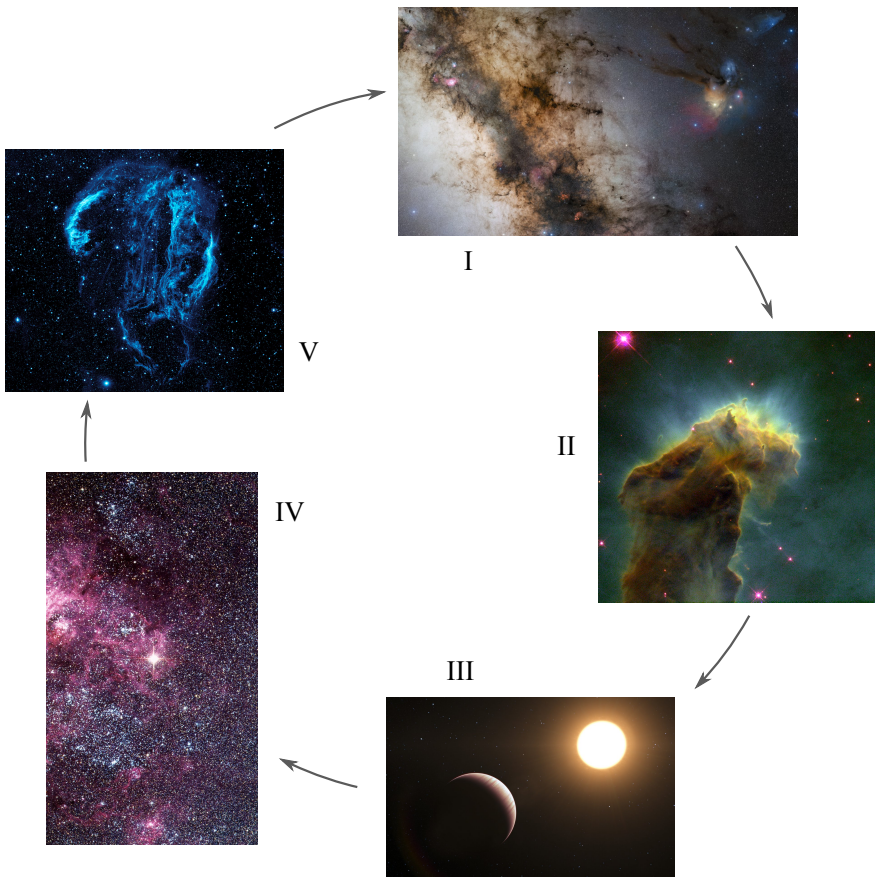

Figure 3.1. Illustration of the life cycle of massive stars.

Image credits:
I. ESO/S. Guisard (www.eso.org/~sguisard), CC BY 4.0†
II. NASA
III. ESO/L. Calçada, CC BY 4.0†
IV. ESO, CC BY 4.0†
V. NASA/JPL-Caltech
†Creative Commons Attribution 4.0 International License, http://creativecommons.org/licenses/by/4.0/

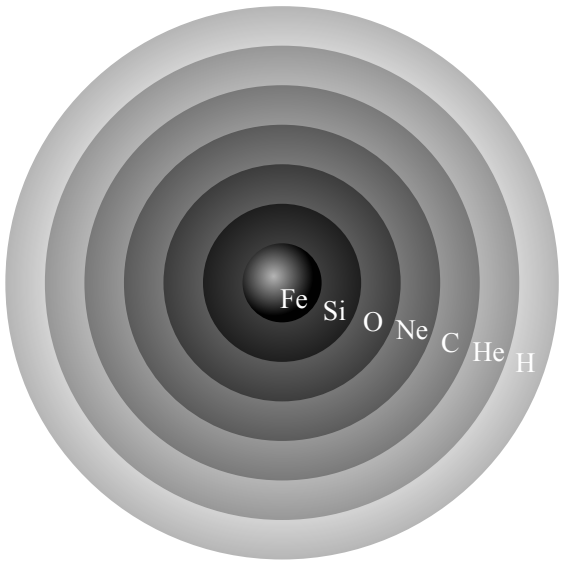

Figure 3.2. Cross-section of a massive star showing the 1D model with stratified layers of individual nuclear burning stages. The thicknesses of the different layers are also not to scale. The size of the iron core is on the order of 10^4 km and the radius of the star is on the order of 10^8 km.

the evolution of stars relies on 1D models and simplified treatments of the involved physics. This approach has successfully described many of the general properties of stars. They are essentially self-gravitating clouds of plasma with high enough temperatures and pressures in the inner regions to sustain thermonuclear fusion. These simplified 1D models predict that the structure of stars is stratified with progressively heavier elements toward the center. However, the evolution of the late stages of massive stars is more complicated than what is captured by the simplified 1D models. The most important parameters are initial mass, rotation, metallicity, and the effects of magnetic fields. In addition, many massive stars evolve as a part of an interacting binary system. To simulate these processes, it is necessary to capture physics ranging from very short to very long spatial and temporal scales. These factors make detailed descriptions of stellar evolution very challenging.

The following stages that involve the explosion and subsequent evolution of the young SNR are explained in more detail in Sections 3.2–3.4. Here, it is simply noted that the final fate of the supernova is that the remnant fades away and merges with the ISM. The end result is that much of the material of the star is returned to the ISM. This is one of the main drivers of the chemical evolution of the Universe (Woosley et al., 2002). The kinetic energy deposited into the ISM also helps trigger the formation of the next generation of stars and planets. The SNR evolution spans over timescales of millions of years and the remnants expand to radii on the order of 100 ly (Vink, 2012). An interesting point is that SNe occur roughly once every century in galaxies similar to the Milky Way. From these numbers, it is clear that SNRs will cover a large fraction of the total volume of a galaxy (McKee and Ostriker, 1977). This implies that SNRs are vital for shaping the ISM environment in galaxies.

3.2 Core Collapse and Bounce

The study of SNe from the onset of core collapse to an outward explosion has received much attention over the past decades (Janka, Marek and Kitaura, 2007; Janka, Langanke, Marek, Martínez-Pinedo and Müller, 2007; Janka, 2012; Burrows, 2013; Müller, 2016; Janka, 2017). CCSNe are termed core collapse because they are triggered by the core of the star crossing a mass limit determined by the electron degeneracy pressure. Degeneracy pressure arises from the Pauli exclusion principle, which states that fermions cannot occupy the same quantum state simultaneously. Effectively, this implies that astrophysical objects that are dense enough experience an additional pressure as a result of quantum mechanics, which prevents further gravitational compression. When the limit is crossed, the core cannot withstand

the force of gravity. This process is self-enhancing, so once the collapse has started, the core and all outer layers keep collapsing into a neutron star, which halts the contraction and expels the outer layers and appears as a SN to observers. However, if neutron degeneracy pressure is overcome, the star keeps contracting into a black hole.

Once the core collapse is initiated, the contraction increases the temperature. The temperature increase leads to photodissociation of heavy nuclei into α-particles, and, subsequently, fissioning α-particles into individual nucleons, effectively depositing the energy released when fusing the heavy nuclei. The photodissociation acts as an energy sink, which lowers the temperature and facilitates further collapse. Thus, these effects combine to form a positive feedback loop. Throughout this process, electrons are captured by protons, which forms neutrons and electron neutrinos. The neutrinos are able to escape freely during the collapse phase. The collapse continues until neutron degeneracy pressure dominates, halting the collapse and forming a neutron star, or, if neutron degeneracy is overcome, contracting further into a black hole.

Gravitational Potential Energy

Fundamentally, CCSNe are powered by gravitational potential energy released by the contracting core. The energy liberated by explosive nucleosynthesis contributes at most a small fraction of the released energy (Burrows, 2013). A simple back-of-the-envelope calculation can be made by computing the change in gravitational potential energy of the core. For a typical initial radius of 10,000 km, final radius of 10 km, and a mass of 1 $M_\odot$, Equation (2.4) gives a change of binding energy of more than 10^{53} erg. Thus, the remaining question is how to convert approximately a few percents of the released gravitational potential energy into the observed SNe (Section 3.3).

A characteristic of CCSNe is the bounce shock associated with the rebound of the infalling matter when the proto-neutron star (PNS) is formed. When the core density reaches nuclear densities of $\sim 10^{14}$ g cm^{-3}, neutron degeneracy pressure overtakes the other forces at play and the equation of state suddenly stiffens within less than a millisecond (Burrows, 2013). This is potent enough to reverse the infall to some degree by sending a shock outwards and was thought to possibly prompt the ejection of the stellar mantle, i.e. trigger the SN explosion. Therefore, the bounce-shock mechanism attracted much attention in the 1980s (Bethe, 1990).

However, the current consensus is that bounce-shock alone is insufficient to describe the explosion of any star (Janka, 2012; Burrows, 2013; Müller,

2016). The shock is launched from an enclosed mass of ∼0.5 $M_\odot$, keeps propagating outward for ∼70 ms, and reaches a peak radius of 100–200 km before turning into an accretion shock with negative radial velocity. Energy is tapped out of the escaping shock through photodissociation of infalling heavy nuclei. Practically all modern simulations indicate that this is the final fate for the bounce-shock mechanism, i.e. stagnation deep inside the core of the star (e.g. Mezzacappa et al., 2001). Nevertheless, even though the bounce-shock mechanism fails to explode the star, it has important consequences for subsequent processes.

3.3 Explosion Mechanisms

3.3.1 Delayed Neutrino Heating

Mental Image

Presentations (especially visualizations) of SNe often focus on the high luminosity, which is to say the electromagnetic radiation. However, the total radiated energy in ordinary SNe is on the order of 10^{49} erg (e.g. Lyman et al. 2016, Dastidar et al. 2018). This is only around 1 % of the total kinetic energy, which is on the order of 10^{51} erg (e.g. Janka et al. 2017 and references therein). The kinetic energy is also the energy that is customarily referred to as the explosion energy. As shown in Section 3.2, the total liberated energy is on the order of 10^{53} erg. Approximately 99 % of this energy escapes as neutrinos whereas the small fraction that is absorbed powers the explosion.
The timescales are also quite different from the intuitive notion of an explosion. Whether or not the star collapses into a black hole, or explodes and leaves a neutron star is determined during the first second after the bounce. The structure of the ejecta is determined during the first few hours. The hydrodynamic processes of the heated ejecta are in some aspects quite similar to boiling water. All of this happens before the SN becomes immensely bright, which is what SNe are most known for. The radiation escapes on timescales of tens of days because of the time it takes for photons to escape the thick envelope and the continuous expansion of the ejecta.

Much of the modern research has been committed to the study of the revival of the initial bounce shock through neutrino heating, often referred to as the delayed neutrino-driven mechanism (Colgate and White, 1966; Arnett, 1966; Bethe and Wilson, 1985). Neutrino heating is the frontrunner

among the studied explosion mechanisms even though currently far from all progenitors can be satisfyingly modeled.

In the wake of the bounce shock, the so-called gain radius emerges. For radii smaller than the gain radius, neutrinos cool, whereas neutrinos heat for larger radii (Bethe and Wilson, 1985). Eventually, the pressure behind the shock is sufficient to give rise to an outward expansion, effectively reviving the stalled shock. The amount of dissociated nucleons exposed to strong neutrino heating behind the shock keeps increasing because of matter being accreted through the shock front and an increasing shock radius. These effects combined turns neutrino heating into a partly self-enhancing runaway process (Müller, 2016).

It has been concluded that neutrino heating is insufficient to explode stars in 1D (e.g. Fischer et al. 2010). However, it is established that SNe are highly asymmetrical, being anisotropic from the very first moments of explosions as shown in Figures 1.1 and 1.2. Whether or not multi-dimensional, particularly 3D, simulations result in successful explosions through neutrino driving is still an area of active research. It has been shown that convection and instabilities lower the luminosity required for explosion in multi-D by 12–50 % (recent work seems to favor values in the lower end of the interval), with respect to 1D (Nordhaus et al., 2010; Hanke et al., 2012; Fernández, 2015; Müller and Janka, 2015; Müller et al., 2016).

Going beyond 1D qualitatively alters the conditions for effects such as convection and non-radial sloshing motions. These hydrodynamical instabilities evolve during the very first moments of the explosion and play a critical role for neutrino driving (Herant et al., 1992, 1994; Burrows et al., 1995; Fryer and Warren, 2002, 2004). Comparisons between 1D and 2D simulations focused on instabilities have been made, showing that 2D instabilities can be decisive for a successful explosion (Buras et al., 2006; Marek and Janka, 2009). However, it is possible to find plenty of cases of both failed (e.g. Hanke et al., 2013; Tamborra et al., 2014) and successful (e.g. Takiwaki et al., 2014; Melson et al., 2015; Lentz et al., 2015) explosions in 3D.

How instabilities aid neutrino driving is a highly complex process. Effects such as radial Rayleigh-Taylor fingers convect freshly heated material from the gain layer further out towards the shock and lets newly infallen matter down into the heating region. This leads to an overall increase of temperature and pressure in the gain region, which in turn pushes the shock outwards. Altogether, it is believed that this triggers a self-sustaining feedback loop, which eventually leads to the expulsion of the stellar mantle (Couch and Ott, 2013; Couch et al., 2015). In contrast, the non-radial mass flows dissipate kinetic energy in the form of heat, indirectly boosting the outward, radial expansion and convective activity (Scheck et al., 2008;

Marek and Janka, 2009).

The large-scale asymmetries naturally originate from initial seed perturbations. In particular, it has been advocated that strong seed perturbations in the infalling oxygen or silicon shells indirectly enhances neutrino driving (Arnett and Meakin, 2011; Couch and Ott, 2013; Müller and Janka, 2015; Couch et al., 2015; Müller et al., 2016). A 3D explosion simulation used the 3D initial conditions from Müller et al. (2017) and used 1D initial conditions as a reference. It was concluded that the shock was revived using 3D initial conditions and that the 1D initial conditions yield no explosion (Müller, 2016; Müller et al., 2017).

However, there are SNe that are significantly more luminous than standard SNe (see Section 3.7). This is a problem for the delayed neutrino-heating mechanism because neutrino-driven simulations indicate that a few times 10^{51} erg might be an upper limit to the explosion energy that can be achieved. Additionally, even though neutrino heating might be the leading hypothesis, the viability of delayed neutrino heating to explode the less extreme SNe is also not generally accepted.

3.3.2 Other Mechanisms

Magnetorotational mechanism (MRM) is a magnetohydrodynamic effect that was, in its most fundamental form, developed during the 1970s (Bisnovatyi-Kogan, 1970; Ostriker and Gunn, 1971; Meier et al., 1976; Bisnovatyi-Kogan et al., 1976). The basic concept is that a nascent PNS has a high rate of rotation, close to critical rotation of $\sim$1 ms. Any significantly faster rotation would render gravity unable to hold the neutron star together. A strong magnetic field is also required, approximately 10^{15} G or more. Rotational energy from the PNS is then transferred into the mantle, depositing enough kinetic energy into the outer stellar layers for it to be expelled, resulting in a SN explosion. Modern simulations have verified that the outlined process is a viable method for expelling the outer layers (Burrows et al., 2007). It is worth mentioning that MRM may power the progenitors of long gamma-ray bursts (MacFadyen and Woosley, 1999).

However, because MRM requires a high spin, it is relatively straightforward to compare pulsar spins with those predicted by MRM theory. Results show that only less than $\sim$1% of pulsars are possible MRM SN remnants. So, even if MRM is a viable mechanism, it is constrained to a very small population. Therefore, an attractive hypothesis is that MRM powers the most luminous SNe that have the most rapidly rotating cores (Burrows, 2013).

Alternative suggestions to neutrino heating for standard SNe involve collapse-induced thermonuclear explosions (Burbidge et al., 1957) and jet-driven explosions (Soker, 2010). Kushnir and Katz (2015) showed that thermonuclear explosions are possible for some (tuned) progenitors in 1D simulations. More finely tuned models indicate that it is possible to obtain kinetic energies in the range 10^{49}–10^{52} erg in 2D thermonuclear explosion simulations (Blum and Kushnir, 2016). The jet mechanism relies on the formation of jets by the material infalling onto the nascent neutron star just after the core collapse, which then explode the star (Soker, 2017*a*,*b*).

3.4 Supernova Remnants

The transition of a SN to a SNR is often taken to be the time when the emission is dominated by interactions with the surroundings rather than the decay of radioactive elements created by the explosive nucleosynthesis in the SN explosion. SNe eject large amounts of matter into space with typical total kinetic energies of 10^{51} erg. Ejecta masses are normally in the range $\sim$4–20 $M_\odot$. This means that a typical velocity is $\sim$3000 km s^{-1}, which is significantly higher than the sound speed of the surroundings. The result is that a shock wave expands through the circumstellar medium (CSM). The shock surface serves as the effective boundary of a SNR, which includes the shock and the ejecta inside of it. Fundamentally, the SNR covers the timespan during which the kinetic energy of the bulk motion is reprocessed into other forms (Lopez and Fesen, 2018).

The evolutionary stage of a SNR is often categorized depending on the dominating physical processes (Draine, 2011; Vink, 2012). The important physical parameters for the evolution of the ejecta are the density, pressure, temperature, and kinetic energy. This is further complicated by asymmetries in the ejecta and surrounding material. It is possible that parts of the ejecta are still expanding freely whereas other parts of the ejecta already have lost most of its kinetic energy.

The free-expansion (or ejecta-dominated) phase is the first phase after the explosion and lasts roughly until the swept-up mass exceeds the ejecta mass. This is the only phase relevant to this thesis. Typical velocities of the fastest SN ejecta is on the order of 10^4 km s^{-1}, which is significantly higher than the local sound speed of $\sim$10 km s^{-1}. Furthermore, the ejecta density at early phases is much higher than the CSM density. This results in a blast wave propagating outward while the ejecta expands approximately freely. For a given ejecta mass $M_{\rm ej}$, CSM density n_0, and explosion energy E_{51}, it is possible to compute the time at which the swept-up mass exceeds the

ejecta mass (Draine, 2011)

$$t_1 = 186 \text{ yr} \left(\frac{M_{\rm ej}}{M_\odot}\right)^{5/6} E_{51}^{-1/2} n_0^{-1/3}. \quad (3.1)$$

Once the swept-up mass is comparable to the ejecta mass, the pressure in the shell of shocked CSM roughly exceeds the thermal pressure of the ejecta. This sends a reverse shock inward, which slows and heats the ejecta. It is worth pointing out that the reverse shock propagates inward as measured in mass coordinate, which means that it is reaching more of the inner mass. However, the reverse shock could still be expanding outward in space, but with a lower radial velocity than the ejecta at that radius. Throughout the free-expansion phase, the density drops as t^{-3}, and the part of the ejecta inside of the reverse shock cools due to adiabatic expansion until the reverse shock reaches it and shock heats it.

Cas A (Figure 1.1, left) is an example of a relatively young and nearby SNR formed by a SN that was possibly observed by John Flamsteed on 16 August 1680 (Flamsteed, 1725; Kamper, 1980; Hughes, 1980; Ashworth, 1980). The neutron star created by the SN was detected in the first light images of *Chandra* (Tananbaum, 1999; Pavlov et al., 2000; Chakrabarty et al., 2001) and does not contribute to the emission of the SNR. This means that the radiation is powered by the conversion of kinetic energy through CSM interactions. In contrast, most of the energy input in the Crab Nebula comes from the Crab Pulsar (Figure 1.1, right).

In Cas A, the X-ray emission is mainly bremsstrahlung emission that originates from gas heated by the reverse shock. The UVOIR is instead dominated by line emission. In the shocked region, the atoms are ionized by collisions with thermal electrons. The unshocked interior material is photoionized by UV and X-ray photons from the shock-heated gas with temperatures of several million degrees Kelvin (Milisavljevic and Fesen, 2015). Cas A is a strong synchrotron source and is the brightest radio (below 100 GHz) source outside of the solar system.

3.5 Compact Remnants

The compact remnants of SN explosions are expected to be neutron stars or black holes. Neutron stars are primarily characterized by their mass, radius, spin (rotational period), and magnetic field strength, whereas only the mass and spin are of astrophysical relevance for black holes. In addition to the characteristics that are intrinsic to the object, the kick (velocity imparted during the explosion) and interaction with the surroundings are important observational properties and laboratories for extreme physical phenomena.

A successful CCSN requires the formation of a neutron star, but it is possible that a small fraction of all SNe are fallback SNe (e.g. Ertl et al., 2016; Sukhbold et al., 2016). Fallback SNe are those that form a neutron star but subsequent fallback of material onto the neutron star makes it collapse into a black hole. These SNe are predicted to be fainter than the SNe that form stable neutron star remnants. It is also possible for a massive star to collapse into a black hole with no associated explosion. These black holes are referred to as direct collapse black holes and the collapses are classified as failed SNe, which are not strictly a type of SNe. Detecting stars the directly implode into black holes is much more challenging. No unambiguous detection has been made but two candidates have recently been reported (Reynolds et al., 2015; Adams et al., 2017).

One of the predictions for these formation channels is that successful explosions should leave neutron stars with masses of 1–2 $M_\odot$ and the black holes should generally have masses above 5 $M_\odot$. The mass gap between 2–5 $M_\odot$ is thus simply a consequence of the lack of formation channel for objects in the mass gap, which most likely would be black holes. There are relatively robust observational evidence of the mass gap (Farr et al., 2011) and it was replicated reasonably well in a study of remnants in 200 CCSN simulations by Sukhbold et al. (2016).

3.5.1 Neutron Star Properties

Neutron stars constitute a very diverse group of objects but they all share some general properties. Neutron stars have masses in the range 1–2 $M_\odot$, radii of 10–13 km, and spin periods of a few milliseconds to tens of seconds (Özel and Freire, 2016). Because of general relativistic effects, the quantities are dependent on where the measurement is performed and how much internal energy that remains contained by the neutron star (see Section 2.3). A very rough estimation of the difference by measuring the intrinsic properties is a relative change of 20 % for most quantities.

Neutron stars also interact with the environment, which is the supernova remnant for young neutron stars. The surface magnetic field strengths of neutron stars are ranging from 10^9 to 10^{15} G. The magnetic field is often modeled as a rotating dipole in vacuum (Shapiro and Teukolsky, 1983), but more accurate descriptions are still being developed (e.g. Spitkovsky, 2006). The magnetic fields act on the environment because neutron stars are rotating and the magnetic and rotational axes are generally not aligned. Faucher-Giguère and Kaspi (2006) estimated that the birth periods of typical pulsars are 300 ± 150 ms. We note that the value is based on available observations of pulsars and that it is model-dependent.

Typical natal kick velocities of pulsars are on average ∼400 km s^{-1} but can be even larger than 1000 km s^{-1} in some cases (Hobbs et al., 2005; Faucher-Giguère and Kaspi, 2006). A possible explanation for the kicks is that the ejecta is expelled asymmetrically, which requires a velocity to be imparted to the neutron star to conserve momentum (Scheck et al., 2006; Wongwathanarat et al., 2010; Janka, 2017). Thus, kicks serve as a probe of the explosion mechanism, but also complicates association of older neutron stars with their birth SNR.

3.5.2 Accretion

Accretion is the process by which material falls onto a central object (Frank et al., 2002). It is clear that infalling material would not emit radiation unless accretion processes transform kinetic energy into radiation. Gravity is the attractive force that pulls material inward but in practice, the process is limited by angular momentum transfer and interactions within the infalling material, which is where the energy is reprocessed into electromagnetic emission. This also makes it one of the very few ways that black holes manifest themselves. It is worth mentioning that accretion is not limited to the accretion of matter onto neutron stars and black holes. Accretion processes are also responsible for the formation of galaxies, stars, and planets.

Accretion Efficiency

In the context of compact objects, accretion is important because it is one of the most efficient processes of converting rest mass energy to electromagnetic energy. Efficiency is usually measured in terms of an efficiency parameter η defined as the fraction of rest mass energy released [see Equation (2.1)]. A comparison between different mechanisms can be made. The efficiency of chemical reactions such as burning of coal is $\sim 10^{-8}$ %, that of nuclear fusion, specifically $4H \rightarrow He$ (a typical stellar process), is ∼0.7 % whereas a typical value for accretion is ∼10 %.

Compact objects that are actively accreting material are luminous electromagnetic sources. The radiation originates from an accretion disk or, for neutron stars only, from interactions on the surface. The most common characteristics of accretion are X-ray emission and variability on short timescales. The shortest timescale is approximately determined by the light crossing time, i.e. the size of the object divided by the speed of light.

Accretion could occur in different types of environments. For young compact objects, the accreted material is most likely from the SN ejecta.

This is called fallback accretion and could be occurring continuously from the SN explosion moment until thousands of years later (Rees, 1988; Phinney, 1989; Evans and Kochanek, 1989). For older objects, a more likely source of material is a binary companion that evolves into a stellar evolution stage where it expands. This expansion could cause the outer parts to be more strongly attracted by the binary compact companion. A result of this is the expanding star starts losing material, which is accreted by the compact object. The accretion process is fundamentally the same in both cases even though the situations are different.

3.5.3 Pulsars

The term pulsar was originally coined to describe a mysterious object that was observed to emit radio pulses at a regular interval of 1.33 s (Hewish et al., 1968). This is a result of the combination of the strong magnetic fields with the short rotational periods. The emission is observed to pulsate because the radiation is beamed along the axis of the magnetic dipole. This means that emission is observable from Earth only when the beams sweep our line-of-sight. A consequence of this is that many neutron stars should have beams of radio emission that are not observable from Earth, but another possibility is also that not all neutron stars are radio pulsars.

It was later discovered that the pulsating emission can be observed in virtually all wavelengths for some objects. A notable example is the neutron star that resides inside the Crab Nebula (Bühler and Blandford, 2014), which has a period of 34 ms today. This corresponds to photon wavelengths on the order of 10^7 m, which essentially makes the Crab the "megawave oven" counterpart of 10^{29} kitchen microwave ovens (Condon and Ransom, 2016). In the most simple model, this energy is tapped from the rotational energy of the neutron star. A consequence of this is that neutron stars are constantly slowing down while emitting long-wavelength radiation.

Pulsars can increase their spin rate if they acquire angular momentum from an external source. The fastest spinning pulsars are the millisecond pulsars (MSPs) with periods less than approximately 10 ms. The prevailing explanation for their high spins is that they are spun-up ("recycled") by accretion from binary companion stars (Alpar et al., 1982; Radhakrishnan and Srinivasan, 1982). The accreted material could then bury the magnetic field, which allows the pulsars to keep their high spin. When the binary companion has died, only the millisecond pulsar remains observable.

3.5.4 Thermal Surface Emission

All neutron stars are also expected to emit thermal emission from the surface. The first cooling stage of neutron stars is dominated by neutrino emis-

sion from the core. This means that the core temperature evolves almost independently of the crust and that the core cools faster than the crust. The neutron star then enters a stage of thermal crust relaxation when the cooling wave from the core reaches the surface. This happens on a timescale of a few years when the age of the neutron star is 10–100 years. The surface temperature during these early stages is expected to be on the order of millions of Kelvin. Observations of thermal relaxation would provide clues to the physics of the interior of neutron stars (Gnedin et al., 2001; Shternin and Yakovlev, 2008; Page et al., 2009).

One class of neutron stars, called central compact objects (CCOs), are observed to only emit thermal radiation, show no signs of pulsar activity, and are associated with SNRs. Spin-down rates of three CCOs have been measured to be low, which implies low external magnetic dipole fields of approximately $< 10^{11}$ G (Halpern and Gotthelf, 2010; Gotthelf et al., 2013). This would be approximately an order of magnitude weaker than for most of the observed pulsars (Manchester et al., 2005; Luo et al., 2015). Some CCOs display anisotropic surface temperatures (Halpern and Gotthelf, 2010; Gotthelf et al., 2013; Bogdanov, 2014; Rea et al., 2016). A possible explanation for temperature anisotropies is that a stronger magnetic field that affects the thermal properties is trapped inside the neutron star by fallback accretion in the past (Ho, 2011; Bernal et al., 2013; Perna et al., 2013; Bogdanov, 2014).

3.6 3D Structure of SNe

Most of stellar evolution is typically assumed to be an approximately spherical process. However, it is immediately clear from observations of SNRs that they are clearly asymmetric (Hwang et al., 2004; Grefenstette et al., 2017; Larsson et al., 2016; Abellán et al., 2017). In addition to the asymmetric morphology, the mixing of materials is also important. Mixing refers to the breaking of the stratified radial structure (see Figure 3.2) and blending of regions of different compositions. The mixing is important for the explosive nucleosynthesis, for the emission from subsequent phases, and as an important property of the explosion mechanism. The small-scale (microscopic) mixing is also important for the formation of dust and molecules in the ejecta. The spatial distributions of the heavy metals are sensitive probes of the explosion mechanism because they are synthesized in the innermost regions close to the explosion engine.

Exactly how and when the spherical symmetry is broken is an area of active research. Hydrodynamic instabilities in neutrino-driven SN simulations are capable of producing asymmetries that are qualitatively similar to observed SNRs (Hammer et al., 2010; Janka, 2017; Wongwathanarat et al.,

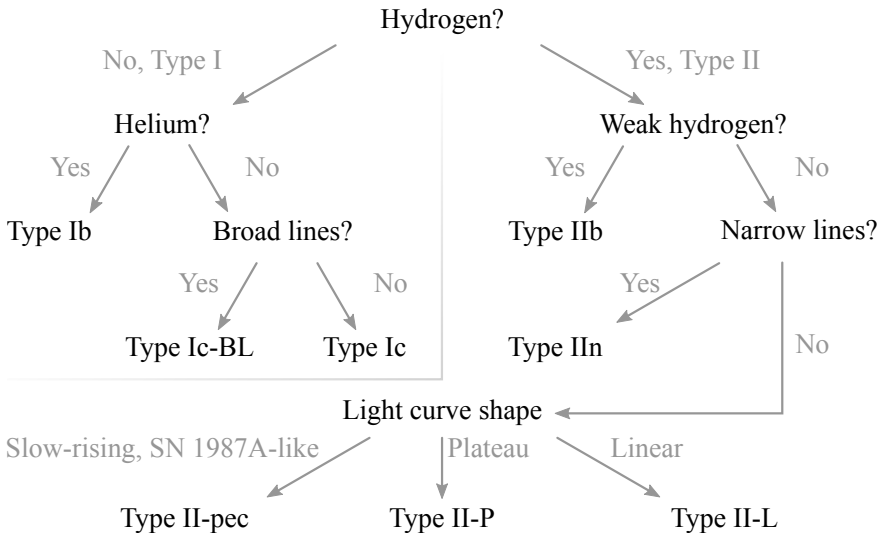

Figure 3.3. CCSN classification scheme. See Section 3.7 for more details on the different SN type and their progenitors.

2017). These asymmetries can develop from almost spherical progenitor models, but it is also possible that the instabilities developed during the explosion are seeded by violent convection in the last stages of the evolution of the progenitors (Couch et al., 2015; Müller et al., 2017).

The clear breaking of all spatial symmetries on many length scales from the very first moments of explosion can be clearly seen in Figure 1.2. The radial convective instabilities, i.e. Rayleigh-Taylor instabilities, on large scales effectively transports ejecta from deep within the core through the outer hydrogen and helium layers resulting in strong mixing and breaking of the stratification developed throughout stellar evolution (Figure 3.2). Typical velocities for the bulk of the iron-group elements are in the range 1000–2000 km s^{-1}. However, observations have shown that a smaller fraction is accelerated to significantly higher velocities (Arnett et al., 1989; Grefenstette et al., 2017). Velocities up to 4500 km s^{-1} for several 10^{-3} $M_\odot$ of ^{56}Ni and other iron-peak elements have also been found in simulations (Hammer et al., 2010).

3.7 Types of Supernovae and Their Progenitors

Even the SNe that arise from the collapse of the iron core of massive stars are subdivided into several subclasses based on the observed properties. The classification scheme (see Figure 3.3 for an illustration) is important because SNe are often referred to by their classes. The label also carries information about different physical and observational properties. The different types are also closely related to different progenitor types. Much effort has been devoted to the association of different types of SNe with observations of different progenitors, but this is a challenging task and is relatively certain only for some classes (Smartt, 2009). Most of the defining properties are based on features in optical spectra and light curves. A review of the classification of all classes of SNe was recently made by Gal-Yam (2017). It is worth emphasizing that capitalization is important (i.e. the labels are case sensitive).

The SNe that show strong signs of hydrogen are classified as Type II SNe. Most of these are Type II-P (plateau) SNe. The plateau refers to a period after the peak during which the brightness stays relatively constant. Those that show a linear decline post-peak are instead termed Type II-L. The decline rate is practically always measured in magnitudes per unit time, so "linear" actually refers to an exponential decline in flux. There are also SNe that initially show hydrogen signs but later transition into strong helium lines. These are denoted Type IIb.

The Type II-P are thought to originate from red supergiants (RSGs). Red here refers to the surface color and is essentially a measure of temperature. The density and radii have important consequences for the observed emission from SNe. A simplified picture is that SN progenitors are very luminous, which means that red stars need much larger radii to emit the same amount of power as a hotter star. Therefore, RSGs have radii of 1000 $R_{\odot}$, whereas blue supergiants (BSGs) have radii of a few times 10 $R_{\odot}$. This is primarily a manifestation of different densities because the total masses of BSGs and RSGs are overlapping.

Type IIb SNe are explosions of stars that have lost much of their hydrogen envelope. It is possible that Type II-L also represent a class of SNe that have lost part of the hydrogen. The hydrogen could be continuously shed off by the star through its evolution or it could be reduced through interactions with a binary companion. The consequences for the SN explosion are that the ejected mass is lower and the expansion velocity is higher. Both of these factors decrease the optical depth of the ejecta and allows more emission to escape earlier.

CCSNe can also lack signs of hydrogen, in which case they are classified as Type Ib. Additionally, there is a Type Ic class for the SNe that also show no signs of helium. These are thought to have lost their outer envelopes through binary interactions. This strips off the lighter elements and only leaves the heavier elements in the inner regions. For completeness, there is also a class called Type Ia, but these are not the result of core collapses in a massive star.

There are also many more subclasses, such as Type Ic-BL (broad-lined), superluminous SNe (SLSNe), Type IIn (narrow), and Type II-pec (peculiar). Type Ic-BL are similar to regular Type Ic but show broader spectral lines and are thought to be connected to long-duration gamma-ray bursts. Type IIn SNe show narrow hydrogen lines that arise from ejecta interacting with the CSM. SLSNe are simply more luminous than normal SNe, often by more than a factor of 100 (Gal-Yam, 2018). Both Type IIn and SLSNe are classes that encompass SNe of more than one physical origin. The Type II-pec are sometimes also called long-rising, slow-rising, or SN 1987A-like (after the archetype SN 1987A). In contrast to Type II-P, these originate from BSGs and possibly also intermediate yellow supergiants (Taddia et al., 2016). Their slow rises are results of their more compact structures.

A final note is that these definitions are not clear-cut. For example, it has been argued that very weak signs of hydrogen can be seen in spectra of Ib SNe and that these should be included in the Type IIb class. Additionally, the distinction between Type II-P and II-L is more continuous than what is typically presented.

3.8 SN 1987A

SN 1987A (Figure 3.4) was observed to explode on 1987 February 23 (Kunkel et al., 1987) and has been thoroughly studied ever since (for reviews, see Arnett et al., 1989; McCray, 1993; McCray and Fransson, 2016). What makes SN 1987A unique is that it is located in the Large Magellanic Cloud, which makes it the closest observed SN since Kepler's SN in 1604 (Kepler, 1606). Consequently, SN 1987A is the only SN that allows astronomers to perform detailed observations at late times and also allows us to detect much fainter components that are otherwise too weak to be observed. For example, it has been possible to spatially resolve the evolution of SN 1987A (e.g. Wang et al., 2002; Larsson et al., 2016; Abellán et al., 2017) and it is clear that the outer layers are powered by CSM interactions rather than radioactive decay (Larsson et al., 2011). A mosaic of this evolution is shown in Figure 3.5.

Figure 3.4. Image of SN 1987A. The triple-ring structure consists of material expelled by the progenitor before the explosion and the rings are now shining brightly as a result of interactions with the SN ejecta. Most of the ejecta by mass is located in the central white bright spot. The two very bright points that are almost co-axial with the triple-ring nebula are just two stars unrelated to SN 1987A and happen to be projected close to SN 1987A.

Image credit:
NASA, ESA, and R. Kirshner (Harvard-Smithsonian Center for Astrophysics and Gordon and Betty Moore Foundation) and P. Challis (Harvard-Smithsonian Center for Astrophysics)

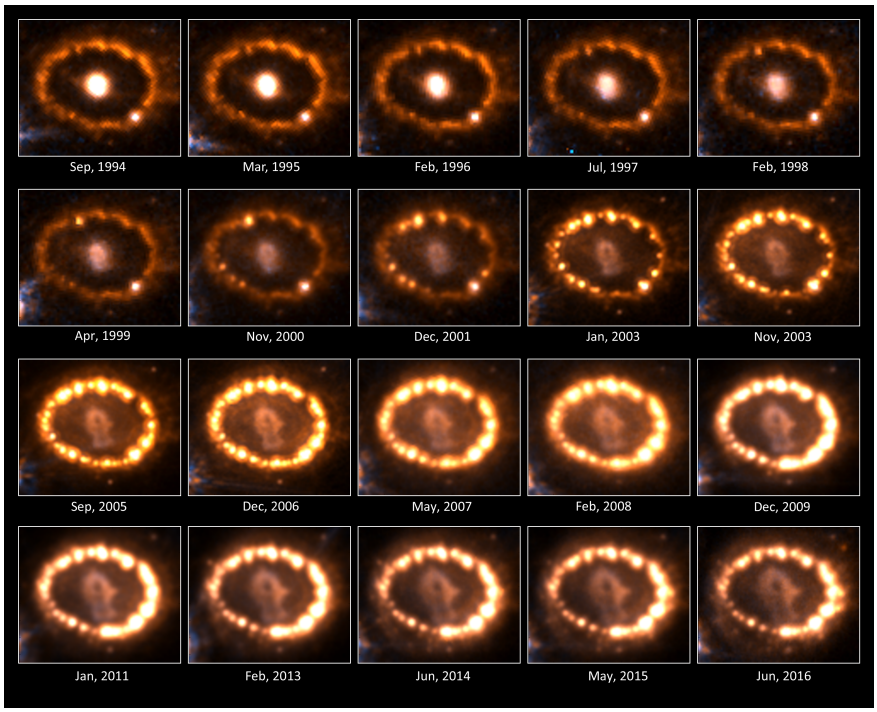

Figure 3.5. Mosaic showing the evolution of SN 1987A from 1994 to 2016. The images are optical images from the *Hubble Space Telescope*. The ring is often called the equatorial ring and is clearly structured on small scales. The ring increases in brightness because the ejecta from the explosion (the clearly evolving central point) slowly collides more violently with the ring, which heats it and makes it brighten.

Image credit:
Josefin Larsson

Additionally, it is the only CCSN where the early radioactive emission has been observed in X-rays and gamma-rays (e.g. Dotani et al., 1987; Sunyaev et al., 1987; Matz et al., 1988), which is used for the analysis in Paper III. One of the important implications of these observations is that the radioactive material must have been mixed from the core where they are formed to the outer layers (e.g. Pinto and Woosley, 1988). Large amounts of dust have been detected in the ejecta (Matsuura et al., 2011; Indebetouw et al., 2014; Matsuura et al., 2015), which implies that CCSNe could be important dust factories. Another consequence of the dust is that our view of the innermost regions is partly obscured in UVOIR. This is very important for our conclusions in Paper I.

Three rings that form an hour-glass shape can be seen around SN 1987A, sometimes called the triple-ring nebula (Figure 3.4). The rings are created by material expelled before the SN explosion and constitute the CSM. The vast majority of the material expelled by the SN remains inside the smallest inner ring. The central ring is the brightest at all wavelengths and is currently violently interacting with the ejecta. It is assumed to mark the equator of the progenitor and is often called the equatorial ring. The two outer rings are much fainter and are seen in some optical images. There are also two very bright stars that are close to SN 1987A (in sky projections) that are unrelated to SN 1987A. These stars are sometimes referred to as star 2 and 3, where star 1 would be Sanduleak -69° 202 (Walborn et al., 1987). Unintuitively, star 3 is the one closer than star 2, possibly because star 2 was more easily distinguishable in early images.

The progenitor was identified as Sanduleak -69° 202, which was a BSG (West et al., 1987; White and Malin, 1987; Kirshner et al., 1987; Walborn et al., 1987). Sanduleak -69° 202 was classified as B3 Ia with a temperature of 15,750 K, a radius of 40 $R_{\odot}$, and a luminosity just above 100,000 $L_{\odot}$ (Walborn et al., 1987; Trundle et al., 2007; Smartt, 2009). The identification of Sanduleak -69° 202 as progenitor and that it was a BSG were important to our description of SNe. An important note is that it is still unclear how a star could evolve and undergo core collapse with the observed properties of Sanduleak -69° 202. There are also additional constraints, such as the existence of the triple-ring nebula and its composition. One hypothesis is that SN 1987A is the result of a binary merger 20,000 years before the explosion (Blondin and Lundqvist, 1993; Morris and Podsiadlowski, 2007, 2009; Menon and Heger, 2017; Menon et al., 2019) or a rapidly rotating progenitor (Chita et al., 2008).

Another major milestone associated with SN 1987A was the detection of the prompt neutrino burst, which signaled the formation of a compact object (Hirata et al., 1987; Bratton et al., 1988; Burrows, 1988). This is important because it is a very firm prediction that underpins all of CCSN theory. This

was also the first detection of astrophysical neutrinos and marked the birth of multi-messenger astronomy (if solar neutrinos are excluded). However, no electromagnetic signal from the compact object has been detected and observations are able to put relatively strong constraints on the remaining possibilities. This is the topic of Paper I.

Chapter 4

Observations

This chapter is an overview of key properties for different kinds of astronomical observatories. I cover the entire electromagnetic spectrum because the analyses in Paper I rely on observations spanning practically the entire spectrum. Paper II and III are limited to X-rays and gamma-rays.

It is important to make a distinction between the telescope and the instrument. The instrument refers to the device that detects the photons collected by the telescopes. Many telescopes are equipped with several instruments with very different capabilities. For ground-based telescopes (and in exceptional cases also space-based), the instruments can be upgraded or replaced, which could significantly improve the scientific capabilities of the same telescope. To avoid confusion, some facilities are referred to as observatories (particularly the space-based) and can have several telescopes.

There are several different kinds of astronomical measurements. The most intuitive is imaging, which just means taking a picture of a part of the sky. Of great scientific importance are measurements of spectra. In general, the spectra of different astronomical objects carry much more information than the corresponding images. A problem with obtaining spectra is that it is observationally and technically more challenging. Additionally, photons are also characterized by polarization. Polarimetric information is sometimes used to infer properties about special physical processes that give rise to polarized emission. The aforementioned properties can also be combined, such as integral field spectroscopy (imaging and spectroscopy) or spectropolarimetry (spectroscopy and polarimetry).

Another avenue of analyzing astronomical objects is by observing how it varies over time. This includes SNe that are transients, meaning that they appear and then disappear. But there are also numerous objects in space that are variable, which means that they are persistent sources that have

some properties that change as a function of time. This could, for example, be a change in the accretion rate onto a compact object or the change in observed brightness of a star when an orbiting planet passes in front of it.

4.1 General Properties of Observations

Many general properties of telescopes are similar throughout the electromagnetic spectrum. The most obvious being the size of the telescope or the effective area. Sometimes efficiency is mentioned, which refers to the probability that an incoming photon is detected. To first order, the efficiency is the factor that converts the telescope area to the effective area.

Another important characteristic is the angular resolution of a telescope. This is roughly the minimum angular separation at which two individual objects can be distinguished. It is worth emphasizing that the resolution is rarely set by the pixel size and that it has nothing to do with the total number of pixels, which is what is commonly used as resolution measures for everyday images.

A concept that is closely related to the angular resolution is the point spread function (PSF, or point response). This is how a point source of emission would appear as observed by the telescope. It is useful because many sources at astronomical distances can be approximated as point sources. The shape of PSFs are often similar to Gaussians or the superposition of two Gaussians.

What determines the angular resolution is in some cases technical difficulties related to how the photons are measured. However, a fundamental limit is set by diffraction, called the diffraction limit. Classically, this is the interference that arises when waves encounter an obstacle. The diffraction limit is proportional to the wavelength over the linear size of the object. In the context of telescopes, the size is the telescope. This means that larger telescopes offer sharper images while also collecting more photons.

In addition to the angular resolution, it is also common to refer to the spectral and temporal resolution of an instrument, if applicable. Spectral resolution refers to the accuracy of the measurement of the photon energies and temporal resolution is the accuracy of the photon arrival time measurement. Spectral resolution is typically given by the smallest measurable energy difference ΔE over the photon energy E, or by resolving power, which is the inverse of spectral resolution.

Other properties of astronomical measurements are the exposure and field of view. These are completely analogous to those of everyday photography. Typical astronomical exposures range from hundreds of seconds to weeks. Fields of view also vary over many orders of magnitude. The

smallest pencil-beam observations cover less than 1 arcsec^2 (a grain of sand at a distance of 100 m) to all-sky monitors that cover 2π sr (half the sky).

All observations also suffer from background. This is typically a combination of the noise from the instrument and the emission from other astrophysical sources. A standard step in almost every data reduction is to subtract the background, often by sampling the background from a nearby representative region free of source emission.

A complicated measurement that is an important characteristic of every instrument is its sensitivity. This is essentially the minimum brightness that can be detected in a given observation. It is complicated because it is a non-trivial combination of the resolutions, effective area, efficiency, exposure, background levels, source properties, and where in the field of view it is observed.

The atmosphere also affects observations by absorbing and distorting the incoming light. The most familiar atmospheric window where photons are transmitted is the optical window, which peaks around what humans can see. It extends from photon wavelengths of around 300 nm to 2.5 μm. The majority of all observatories operate in this range. The second big atmospheric window is in radio to sub-mm from around 30 m to 0.3 mm (1 THz). This is why practically all of the big radio dishes are ground-based. There are several narrower windows in the M-band at 5 μm, the N-band between 8 to 13 μm and the Q-band between 17 and 20 μm. These are much less used, partly because the thermal blackbody emission of the atmosphere (around typical temperatures) peak in this range. The remaining wavebands are almost exclusively observed from space, or in rare cases high-altitude airborne or balloon-borne instruments.

Another effect of the atmosphere is that it blurs the view of the skies at angular resolutions below approximately 1 arcsec. This is often called atmospheric seeing and is an effect of the atmosphere being non-homogeneous, which distorts the light through refraction. This is most problematic for the latest and upcoming generations of ground-based optical and NIR telescopes. To correct for atmospheric seeing, a technique called adaptive optics has been developed. This basically means that the atmospheric distortions are measured and small live mechanical adjustments are made to the shape of the mirrors to compensate for the distortions at adjustment frequencies on the order of 1 kHz. One method of measuring the atmospheric distortions is to project a guide "star" using a laser.

Because of the absorption and distortion, it is common to construct observatories at high altitudes. Humidity is also a key parameter when choosing sites because water vapor limits observations in certain bands.

4.2 Different Wavebands

4.2.1 Radio and (sub-)mm

Radio and (sub-)mm observations reveal objects that produce synchrotron emission and dust emission. Examples of synchrotron sources are shocks in SNRs and jets launched by accretion onto compact objects. The cold dust emission peaks toward the shorter wavelengths and is ubiquitous in all galaxies. Other notable observables are the spin-flip of hydrogen at 21 cm, the cosmic microwave background around 1 mm, and several molecular rotational transitions toward shorter wavelengths.

Radio telescopes use large dishes that are relatively easy to construct because the required precision of the dish only needs to be smaller than the wavelength. This means that the collecting area of radio and (sub-)mm telescopes are very large, with single dishes up to 500 m in diameter. However, the long wavelengths also mean that the energy carried by each photon is very low and very large areas are required to reach competitive sensitivities. It is also very uncommon for astrophysical objects to have a large fraction of the total energy output at wavelengths longer than a few millimeters.

Long wavelengths also mean that the diffraction limit is very high, even for the largest telescopes. A method of improving the angular resolution is to measure incoming wavefronts using several dishes and then reconstructing the complete waveforms, a method called aperture synthesis or interferometry (Ryle and Hewish, 1960). The result is that the diffraction limit can be reduced to the diffraction limit of an instrument with a size equivalent to the longest separation between two dishes. The separations between the dishes are called baselines. Even though the diffraction limit is equal to that of the array as a whole, the arrays are typically sparse with a few dishes spread out over a much larger area. This means that there effectively are holes in the synthesized aperture, from which the information has to be reconstructed in the data processing.

Interferometry has been employed in radio for several decades and is currently being pioneered in NIR. However, combining the data from different telescopes at higher frequencies than around 1 THz is much more challenging and is still in its infancy. Two notable instruments in the radio and (sub-)mm range are Karl G. Jansky Very Large Array (VLA, Thompson et al. 1980; Perley et al. 2011) and the Atacama Large Millimeter/submillimeter Array (ALMA, Wootten and Thompson 2009).

4.2.2 Far- and Mid-Infrared

FIR and MIR cover emission from cool material (approximately below standard temperature), and atomic and molecular lines, a notable example is

the H_2O ground state line at 179 μm. This wavelength range is difficult to observe because the relatively long wavelengths require large telescopes in order to achieve angular resolutions comparable to many other wavebands. This is similar to radio, but the difference is that FIR and MIR are absorbed by the atmosphere, which means that observatories must be placed in orbit. Additionally, the detectors need to be cooled to reduce the thermal noise from the detector itself. There are a small number of instruments that operate from airplanes to avoid most of the atmosphere, or in the narrow bands in the MIR where ground-based observations are possible. However, the thermal emission from the atmosphere still results in extremely high background levels that require special observing modes. The *Herschel Space Observatory* (Pilbratt et al., 2010) was a recent large-class FIR mission that was decommissioned in 2013 and the *James Webb Space Telescope* (Gardner et al., 2006) is an upcoming MIR (and NIR) observatory to be launched in 2021.

4.2.3 UV, Optical, and NIR

Out of all wavebands, the UVOIR range is by far the most mature (and oldest, e.g. Copernicus, 1543; Brahe, 1573; Galilei, 1632). It includes the thermal emission of warm material (approximately 300 K to 1 MK) and many well-observed atomic transitions. This includes emission from stars, SNe, SNRs, and accretion onto compact objects.

The images that are taken in UVOIR are in principle similar to everyday photography in many ways. However, one important difference is that astronomical UVOIR observations are almost exclusively in one filter. A filter is simply something that is placed in the optical path and only lets through light within a certain wavelength range. This is because UVOIR CCDs (Boyle and Smith, 1970) are not inherently color sensitive. The reason that common CCDs capture color is because there are sets of three different CCDs with filters corresponding to red, green, and blue. Another way to view it is that every color picture taken by an everyday camera is, in fact, three simultaneous pictures taken in red, green, and blue filters, which combined results in one color image. This is similar to what is done in astronomy, the difference being that astronomical observations are not limited to three filters in the optical part of the spectrum. In contrast, it is common to simply have one R-band (red) image, which is then visualized using an arbitrary colormap.

Spectroscopy is sometimes performed using slits. When the incoming light passes through the narrow opening, diffraction splits the light into different colors, which are then registered using CCDs. More modern instruments are now capable of performing integral field spectroscopy where a

spectrum is extracted from every pixel in the image. What happens under the hood in these instruments is basically the same. The difference is simply that the light that would have landed on one traditional imaging pixel is redirected onto a grating (or equivalent) such that the diffracted spectrum can be recorded by a CCD. Imaging spectroscopy often comes at the cost of another quality, such as reduced field of view or lower angular resolution. Two examples of IFUs are the Multi-Unit Spectroscopic Explorer (MUSE, Bacon et al. 2010) and the Spectrograph for INtegral Field Observations in the Near Infrared (SINFONI, Eisenhauer et al. 2003; Bonnet et al. 2004) at the Very Large Telescope (VLT).

Cosmic rays and other high-energy particles also trigger CCDs. To mitigate the effects of particles in observations, it is common to combine several individual exposures into a final image. The particle interactions will then clearly show up as bright points or streaks in one of the exposures and can easily be removed when compared to the other images. In addition to removing cosmic rays, it is possible to shift the pointing of the telescope between each pointing by what corresponds to fractions of a pixel to a few pixels. This procedure is called dithering. The process results in a sampling of different physical pixels that could have varying efficiency, it fills in gaps between different CCD chips, and possibly also improves the sampling of the PSF. For example, this is performed for all *Hubble Space Telescope* (*HST*) observations in standard operation modes.

4.2.4 X-Rays

X-rays are effectively absorbed by the atmosphere and are only observed from space, or high-altitude balloons and rockets. It is a relatively young field and was initiated by the first X-ray detection of an extrasolar source by Giacconi et al. (1962). X-rays primarily originate as thermal emission from hot gas (above 1 MK) and as non-thermal emission from relativistic electron populations.

The primary detection technology used for X-rays are also CCDs, but they are quite different from UVOIR CCDs. X-ray CCDs are typically sensitive to the photon energy with a spectral resolution of around 10 %. This means that almost all X-ray images have an associated spectrum with each pixel. The number of photons is often very few and it is common to refer to the total number of photons in an observation. Another difference is that the exposures are much shorter and some CCDs use a triggered read out where the pixel is read each time a photon is registered. The exposure times are often called frame times and vary from milliseconds to a few seconds. The cost of each readout is that the detector is not registering

new events during this time. This downtime is often referred to as readout time or deadtime.

Spectral information is not only provided by CCDs. Higher-resolution spectroscopy in X-rays can be performed using either reflection or transmission gratings. The idea is simply to insert a grating that diffracts the incoming light in the optical path that is then readout by a CCD. The resolving powers of gratings are on the order of several hundred. The drawback of gratings is that they lower the effective area. Another detector type for high-resolution X-ray spectroscopy is microcalorimeters, which are used as detectors instead of CCDs. The concept is that an incident X-ray hits a pixel and deposits the energy into heat. This temperature increase can then be accurately measured and gives spectral resolutions comparable to that of the gratings. X-ray microcalorimeters have been flown on both *Suzaku* (Mitsuda et al., 2007) and *Hitomi* (*ASTRO-H*, Takahashi et al. 2016), but were only operational for a very short time due to accidents. The *X-ray Imaging and Spectroscopy Mission* (*XRISM*, formerly *XARM* and *ASTRO-H2*, Tashiro et al. 2018) is the replacement mission of *Hitomi* and will be equipped with an X-ray microcalorimeter.

X-ray telescopes are also very different from telescopes at lower energies. First, there is no primary mirror that is analogous to the primary of optical telescopes. Instead, X-ray optics rely on grazing incidence mirrors. The concept is that the incoming photons are reflected against X-ray mirrors at very small angles, relative to the surface, toward a focus. This setup requires the mirrors to be nearly aligned with the incoming X-rays resulting in a small effective area for each individual mirror but also allows several mirrors to be nested. This technology is used for several X-ray telescopes, such as *NuSTAR* (Harrison et al., 2013; Madsen et al., 2015) and *XMM-Newton* (Jansen et al., 2001).

Alternative technologies to optics using grazing mirrors are coded mask apertures and collimators. Collimators are simply narrowing the field of view to the detectors and are effectively just "photon buckets". This results in no imaging capabilities. Coded masks rely on masking the detector in such a way that it is possible to reconstruct the direction of the photon to some extent and thus offers low-resolution imaging. An advantage is that the field of view and effective area are more scalable.

Dithering can also be performed in X-ray, similarly to UVOIR observations. Space weather can also affect space telescopes. This depends on the orbit and whether or not it is inside the protective magnetosphere of the Earth. For example, the X-ray telescope *Chandra X-Ray Observatory* (*CXO*, Weisskopf et al. 2000, 2002) is placed in an elliptical orbit with an eccentricity of 0.74 that takes it to more than one-third of the distance to the Moon from Earth. As a result of this, one of the standard data reduc-

tion steps is to check for periods of high background, primarily caused by high-energy protons from the Sun. The advantage of such an orbit is that the telescope is eclipsed by the Earth for a much shorter fraction and that longer continuous observations are possible.

Associated with each X-ray observation are a response matrix file (RMF) and ancillary response file (ARF). These describe the probability that an incoming photon is detected at a given energy as a function of true photon energy and the effective area. These quantities are primarily dependent on the off-axis angle but are also functions of many other instrumental quantities such as the temperature of the instrument and the time since launch.

4.2.5 Gamma-Rays

Gamma-ray astronomy is closely related to X-ray astronomy. Examples of gamma-ray phenomena are jets that are aligned with our line of sight, young magnetars, and emission originating from the decay of radioactive elements (Paper III).

A major difference for gamma-ray astronomy is that there are no focusing optics, but collimators and coded masks are both used. At these photon energies, the detection techniques are partly overlapping with the detection techniques of charged particles. Gamma-ray detectors generally have low angular resolution and a high background level compared to other detectors.

One method of detecting gamma-rays is to let it interact with material, form an electron-positron pair, and then measure the shower of secondary particles that are created. From the direction of the secondary shower, it is possible to reconstruct the incident direction and photon energy. This is the technology used by the Large Area Telescope (LAT, Atwood et al. 2009) on board the *Fermi Gamma-ray Space Telescope* (*Fermi*).

There are also semiconductor detectors that detect the electrons and positive ions that are produced when a high-energy photon passes through the material. An example are the high-purity germanium detectors that constitute the SPectrometer onboard *INTEGRAL* (SPI, Vedrenne et al. 2003; Roques et al. 2003) on board the *INTErnational Gamma-Ray Astrophysics Laboratory* (*INTEGRAL*, Winkler et al. 2003). Another type of detector is the scintillator, which is a material that emits flashes of light when excited by high-energy radiation. This is used to detect gamma-ray bursts by the Gamma-ray Burst Monitor (GBM, Meegan et al. 2009) on board *Fermi*.

Lastly, for very-high-energy gamma-rays, there are ground-based telescopes that observe the light emitted by the secondary particle shower induced by the primary gamma-ray. The secondary particles travel at veloci-

ties higher than the speed of light in air, which results in so-called Cherenkov radiation. This is basically the analogue of a sonic boom for light. The High Energy Stereoscopic System (H.E.S.S., Hinton and the HESS Collaboration 2004) is an example of such a telescope.

4.3 Multi-Messenger Astronomy

It is also important to mention that not all astronomical observations are measurements of electromagnetic radiation. Several astronomical objects also accelerate charged particles to very high energies, first detected by Hess (1912). For historical reasons, these particles are called cosmic rays even though they are particles and not radiation. Today, several large facilities are able to detect these energetic particles of astrophysical origins.

Neutrinos are another type of particle that is generated by astrophysical processes. They are not charged and a characteristic trait is that they are very weakly interacting. Because of the different physics involved in both the origin and detection of neutrinos, they are considered a separate channel from cosmic rays. Neutrino detectors are typically large-volume water (e.g. Super-Kamiokande) or ice (e.g. IceCube) detectors.

A fundamentally different method of astronomical observations is gravitational waves. They are disturbances in spacetime generated by the acceleration of masses. Gravitational waves were first indirectly inferred in a binary neutron star system (Hulse and Taylor, 1975; Taylor and Weisberg, 1989), and recently directly detected from a binary black hole merger by the LIGO and Virgo collaboration (Abbott et al., 2016). Gravitational waves and mass are in many aspects the gravitational equivalent of electromagnetic waves (photons) and charge. The main difference being that the gravitational effects are much weaker, which is why only the most massive objects under extreme acceleration generate detectable gravitational waves.

Chapter 5

Summary of the Attached Papers

5.1 Paper I

The compact remnant that is expected to have been formed by SN 1987A has not yet been detected despite more than 30 years of searches. The formation of a compact object is a critical prediction of CCSN theory and SN 1987A offers the best possibility for us to directly confirm this. Since it has not yet been detected, it is important to use the available observations to constrain the remaining possibilities. Of particular interest are the remaining possibilities for a neutron star because this scenario is favored by most theories.

We used recent observations in millimeter, NIR, optical, UV, and X-rays to achieve the most complete coverage possible. One of the major challenges was to model how the emission from a compact object could be reprocessed. This is important because it is likely that much of the original emission from a compact remnant would be absorbed. However, the energy must still escape the ejecta in some form. To model these interactions, we use the X-ray absorption model from Paper II as well as a much more uncertain dust model based on previous research.

The complete physical model constrains accretion, pulsar wind activity, and thermal surface emission from a neutron star. The accretion limits are fairly constraining and rule out many of the theoretical predictions of fallback accretion. The limit on the magnetic field strength and rotation period are more difficult to interpret because of the lack of accurate theoretical predictions. We find that certain dust properties are likely required

just for the thermal surface emission to remain undetected, but this conclusion relies on a number of assumptions. This means that a neutron star remains a possibility, but the remaining parameter space is relatively small. A number of future facilities will provide very interesting observations that have the chance of detecting a neutron star. Of particular interest are the next generation of ground-based optical and NIR telescopes that will have unprecedented angular resolutions and sensitivities, and future ALMA observations of the thermal dust emission. Finally, we simply note that a black hole is fully consistent with observations and that this scenario is, unfortunately, very difficult to verify observationally.

5.2 Paper II

This paper focuses on the X-ray absorption in young SNRs using 3D models from neutrino-driven SN explosion simulations. Young in this context is from ∼100 days to around 1000 years, but these numbers sensitively depend on how much the ejecta interact with the environment. The aim was primarily to study the X-ray absorption but the models are valid to beyond 1 MeV. In contrast to the other papers, we use the SN simulations to model how much absorption we expect to the center of the remnants. Basically, this means that we use the prediction as a model rather than directly testing the accuracy of the model. The absorption to the center is of particular interest because the compact remnant left by a CCSN explosion should reside relatively close to the center.

One of the motivations for this study was that a more detailed model was required to model the X-ray optical depth to the center of SN 1987A for Paper I. We find that the X-ray depth to the center is expected to be very high in SN 1987A at current epochs. It is unlikely that the compact object that was created will be observed directly in X-rays over the next few decades. Furthermore, we apply the model to the CCO in Cas A, for which the importance of ejecta absorption has been discussed but we find that it is negligible. This paper also investigated how much variance that can be introduced by asymmetries, different progenitors, and different SN types. We also conclude that the absorption properties are relatively similar for both the BSG and RSG progenitors. The different density profiles only have a minor impact on the absorption. However, the total mass is a very important factor. Not only does more material imply higher absorption, but it also results in lower expansion velocities and tends to smooth out any asymmetries. We stress that these conclusions rely on a limited number of models and the assumptions that go into the SN simulations and their progenitors.

5.3 Paper III

In this paper, we compare the same 3D models based on neutrino-driven SN simulations with early X-ray and gamma-ray observations of SN 1987A. The early emission refers to the direct and reprocessed emission that originates from the radioactive decay of elements that were synthesized in the explosion. The important physical processes for the radiation transfer are Compton scattering and photoabsorption. The general behavior is that a photon is produced by a radioactive decay with a typical energy of around 1 MeV. In this energy regime, Compton scattering dominates and photoabsorption is negligible. Compton scattering does not destroy the photon but the photon energy is reduced and scattered into a new propagation direction. A large number of interactions and energy reductions slowly shift the photons into the low-energy regime where photoabsorption becomes increasingly important. Photoabsorption stars becoming important below 100 keV but the exponential dependence causes a sharp cutoff around 20 keV. This means that each photon is randomly scattered around inside the ejecta and the question is essentially how much energy the photon manages to escape with or if it gets absorbed.

From the models, it is possible to perform computer simulations of the photon propagation. We compare these predictions with observations of SN 1987A during the first 1000 days. There were numerous space-based and balloon-borne instruments that performed measurements. They provided spectra and light curves in the 10–200 keV range, which captures the emission that has scattered several times before escaping. There are also more limited data available around 1 MeV that shows the temporal evolution of the fluxes of the direct line emission, primarily the two most important lines at 847 and 1238 keV of ^{56}Co.

We find that the model predictions agree well with observed data. There are minor indications that slightly more mixing of the fastest trace amounts of nickel is needed and that the bulk of the nickel is moving away from us faster than what is found in the models. The different non-stripped RSG and BSG progenitors show very similar emission features. The stripped-envelope Type IIb model evolves much faster and is much brighter because of its lower ejecta mass and higher expansion velocities. The asymmetries and 3D structures primarily affect the magnitude of the flux but the shapes of the spectra and light curves are rather insensitive to the viewing direction. We also find that the progenitor surface metallicity determines the low-energy photoabsorption X-ray cutoff, which potentially allows for constraints on the progenitor metallicity. Future observations of the X-ray continuum with *NuSTAR* are able to detect SNe up to 3–10 Mpc and *INTEGRAL*/SPI can measure the direct line emission from SNe within 0.2–2 Mpc.

Acknowledgments

I would like to thank my supervisor Josefin Larsson, and Claes Fransson, for support and guidance. I also want to thank all other colleagues at the Particle and Astroparticle Physics Department.

Bibliography

Abbott, B. P., Abbott, R., Abbott, T. D. et al. (2016), *Physical Review Letters* **116**(6), 061102.

Abellán, F. J., Indebetouw, R., Marcaide, J. M. et al. (2017), *ApJ* **842**, L24.

Adams, S. M., Kochanek, C. S., Gerke, J. R., Stanek, K. Z. and Dai, X. (2017), *MNRAS* **468**, 4968–4981.

Alpar, M. A., Cheng, A. F., Ruderman, M. A. and Shaham, J. (1982), *Nature* **300**, 728–730.

Arnett, W. D. (1966), *Canadian Journal of Physics* **44**, 2553–2594.

Arnett, W. D., Bahcall, J. N., Kirshner, R. P. and Woosley, S. E. (1989), *ARA&A* **27**, 629–700.

Arnett, W. D. and Meakin, C. (2011), *ApJ* **733**, 78.

Ashworth, Jr., W. B. (1980), *Journal for the History of Astronomy* **11**, 1.

Atwood, W. B., Abdo, A. A., Ackermann, M. et al. (2009), *ApJ* **697**, 1071–1102.

Baade, W. and Zwicky, F. (1934), *Proceedings of the National Academy of Science* **20**, 259–263.

Bacon, R., Accardo, M., Adjali, L. et al. (2010), The MUSE second-generation VLT instrument, *in* 'Ground-based and Airborne Instrumentation for Astronomy III', Vol. 7735 of *Proc. SPIE*, p. 773508.

Becker, W., ed. (2009), *Neutron Stars and Pulsars*, Vol. 357 of *Astrophysics and Space Science Library*.

Bernal, C. G., Page, D. and Lee, W. H. (2013), *ApJ* **770**, 106.

Bethe, H. A. (1990), *Reviews of Modern Physics* **62**, 801–866.

Bethe, H. A. and Wilson, J. R. (1985), *ApJ* **295**, 14–23.

Bisnovatyi-Kogan, G. S. (1970), *Azh* **47**, 813.

Bisnovatyi-Kogan, G. S., Popov, I. P. and Samokhin, A. A. (1976), *Ap&SS* **41**, 287–320.

Blondin, J. M. and Lundqvist, P. (1993), *ApJ* **405**, 337–352.

Blum, K. and Kushnir, D. (2016), *ApJ* **828**, 31.

Blundell, S. and Blundell, K. (2010), *Concepts in Thermal Physics*, Oxford University Press.

Bogdanov, S. (2014), *ApJ* **790**, 94.

Boggs, S. E., Harrison, F. A., Miyasaka, H. et al. (2015), *Science* **348**, 670–671.

Bonnet, H., Abuter, R., Baker, A. et al. (2004), *The Messenger* **117**, 17–24.

Boyle, W. S. and Smith, G. E. (1970), *Bell System Technical Journal* **49**(4), 587–593. **URL:** *https://onlinelibrary.wiley.com/doi/abs/10.1002/j.1538-7305.1970.tb01790.x*

Brahe, T. (1573), *De nova et nullius aevi memoria prius visa Stella*, 1 edn, Hafniae.

Bratton, C. B., Casper, D., Ciocio, A. et al. (1988), *Phys. Rev. D* **37**, 3361–3363.

Bühler, R. and Blandford, R. (2014), *Reports on Progress in Physics* **77**(6), 066901.

Buras, R., Janka, H.-T., Rampp, M. and Kifonidis, K. (2006), *A&A* **457**, 281–308.

Burbidge, E. M., Burbidge, G. R., Fowler, W. A. and Hoyle, F. (1957), *Reviews of Modern Physics* **29**, 547–650.
Burrows, A. (1988), *ApJ* **334**, 891–908.
Burrows, A. (2013), *Reviews of Modern Physics* **85**, 245–261.
Burrows, A., Dessart, L., Livne, E., Ott, C. D. and Murphy, J. (2007), *ApJ* **664**, 416–434.
Burrows, A., Hayes, J. and Fryxell, B. A. (1995), *ApJ* **450**, 830.
Cardelli, J. A., Clayton, G. C. and Mathis, J. S. (1989), *ApJ* **345**, 245–256.
Chakrabarty, D., Pivovaroff, M. J., Hernquist, L. E., Heyl, J. S. and Narayan, R. (2001), *ApJ* **548**, 800–810.
Cheng, T.-P. (2005), *Relativity, gravitation and cosmology. A basic introduction*, Oxford University Press.
Chita, S. M., Langer, N., van Marle, A. J., García-Segura, G. and Heger, A. (2008), *A&A* **488**, L37–L41.
Colgate, S. A. and White, R. H. (1966), *ApJ* **143**, 626.
Compton, A. H. (1923), *Physical Review* **21**, 483–502.
Condon, J. J. and Ransom, S. M. (2016), *Essential Radio Astronomy*, Princeton University Press, Princeton, NJ.
Copernicus, N. (1543), *Nicolai Copernici Torinensis de revolutionibus orbium coelestium Libri VI*, 1 edn, Johannes Petreius, Nuremberg.
Couch, S. M., Chatzopoulos, E., Arnett, W. D. and Timmes, F. X. (2015), *ApJ* **808**, L21.
Couch, S. M. and Ott, C. D. (2013), *ApJ* **778**, L7.
Dastidar, R., Misra, K., Hosseinzadeh, G. et al. (2018), *MNRAS* **479**, 2421–2442.
Dotani, T., Hayashida, K., Inoue, H. et al. (1987), *Nature* **330**, 230.
Draine, B. T. (2003), *ApJ* **598**, 1026–1037.
Draine, B. T. (2011), *Physics of the Interstellar and Intergalactic Medium*, Third edn, Princeton University Press.
Einstein, A. (1905*a*), *Annalen der Physik* **322**, 132–148.
Einstein, A. (1905*b*), *Annalen der Physik* **322**, 891–921.
Einstein, A. (1916), *Annalen der Physik* **354**, 769–822.
Eisenhauer, F., Abuter, R., Bickert, K. et al. (2003), SINFONI - Integral field spectroscopy at 50 milli-arcsecond resolution with the ESO VLT, *in* M. Iye and A. F. M. Moorwood, eds, 'Instrument Design and Performance for Optical/Infrared Ground-based Telescopes', Vol. 4841 of *Proc. SPIE*, pp. 1548–1561.
Ertl, T., Janka, H.-T., Woosley, S. E., Sukhbold, T. and Ugliano, M. (2016), *ApJ* **818**, 124.
Evans, C. R. and Kochanek, C. S. (1989), *ApJ* **346**, L13–L16.
Farr, W. M., Sravan, N., Cantrell, A. et al. (2011), *ApJ* **741**, 103.
Faucher-Giguère, C.-A. and Kaspi, V. M. (2006), *ApJ* **643**, 332–355.
Fernández, R. (2015), *MNRAS* **452**, 2071–2086.
Fischer, T., Whitehouse, S. C., Mezzacappa, A., Thielemann, F.-K. and Liebendörfer, M. (2010), *A&A* **517**, A80.
Flamsteed, J. (1725), *Historia Coelestis Britannicae, tribus Voluminibus contenta (1675-1689), (1689-1720), vol. 1, 2, 3*, London: H. Meere; in folio; DCC.f.9, DCC.f.10, DCC.f.11.
Frank, J., King, A. and Raine, D. J. (2002), *Accretion Power in Astrophysics: Third Edition*, UK: Cambridge University Press.
Fryer, C. L. and Warren, M. S. (2002), *ApJ* **574**, L65–L68.
Fryer, C. L. and Warren, M. S. (2004), *ApJ* **601**, 391–404.
Gal-Yam, A. (2017), Observational and Physical Classification of Supernovae, *in* A. W. Alsabti and P. Murdin, eds, 'Handbook of Supernovae, ISBN 978-3-319-21845-8. Springer International Publishing AG, 2017, p. 195', Springer International Publishing AG, p. 195.
Gal-Yam, A. (2018), *ArXiv e-prints* .

Galilei, G. (1632), *Dialogo DI Galileo Galilei Linceo matematico spraordinario dello stvdio DI Pisa.*, 1 edn, Per Gio: Batista Landini, Florence.

Gardner, J. P., Mather, J. C., Clampin, M. et al. (2006), *Space Sci. Rev.* **123**, 485–606.

Giacconi, R., Gursky, H., Paolini, F. R. and Rossi, B. B. (1962), *Physical Review Letters* **9**, 439–443.

Gnedin, O. Y., Yakovlev, D. G. and Potekhin, A. Y. (2001), *MNRAS* **324**, 725–736.

Gotthelf, E. V., Halpern, J. P. and Alford, J. (2013), *ApJ* **765**, 58.

Grebenev, S. A., Lutovinov, A. A., Tsygankov, S. S. and Winkler, C. (2012), *Nature* **490**, 373–375.

Grefenstette, B. W., Fryer, C. L., Harrison, F. A. et al. (2017), *ApJ* **834**, 19.

Grefenstette, B. W., Harrison, F. A., Boggs, S. E. et al. (2014), *Nature* **506**, 339–342.

Halpern, J. P. and Gotthelf, E. V. (2010), *ApJ* **709**, 436–446.

Hammer, N. J., Janka, H.-T. and Müller, E. (2010), *ApJ* **714**, 1371–1385.

Hanke, F., Marek, A., Müller, B. and Janka, H.-T. (2012), *ApJ* **755**, 138.

Hanke, F., Müller, B., Wongwathanarat, A., Marek, A. and Janka, H.-T. (2013), *ApJ* **770**, 66.

Harris, R. (2007), *Modern Physics*, 2 edn, Pearson.

Harrison, F. A., Craig, W. W., Christensen, F. E. et al. (2013), *ApJ* **770**, 103.

Herant, M., Benz, W. and Colgate, S. (1992), *ApJ* **395**, 642–653.

Herant, M., Benz, W., Hix, W. R., Fryer, C. L. and Colgate, S. A. (1994), *ApJ* **435**, 339–361.

Hess, V. F. (1912), *Phys. Z.* **13**, 1084–1091.

Hewish, A., Bell, S. J., Pilkington, J. D. H., Scott, P. F. and Collins, R. A. (1968), *Nature* **217**, 709–713.

Hinton, J. A. and the HESS Collaboration (2004), *New Astron. Rev.* **48**, 331–337.

Hirata, K., Kajita, T., Koshiba, M., Nakahata, M. and Oyama, Y. (1987), *Physical Review Letters* **58**, 1490–1493.

Hix, W. R. and Harris, J. A. (2017), The Multidimensional Character of Nucleosynthesis in Core-Collapse Supernovae, *in* A. W. Alsabti and P. Murdin, eds, 'Handbook of Supernovae, ISBN 978-3-319-21845-8. Springer International Publishing AG, 2017, p. 1771', p. 1771.

Ho, W. C. G. (2011), *MNRAS* **414**, 2567–2575.

Hobbs, G., Lorimer, D. R., Lyne, A. G. and Kramer, M. (2005), *MNRAS* **360**, 974–992.

Hoyle, F. (1954), *ApJS* **1**, 121.

Hoyle, F. and Fowler, W. A. (1960), *ApJ* **132**, 565.

Hughes, D. W. (1980), *Nature* **285**, 132–133.

Hulse, R. A. and Taylor, J. H. (1975), *ApJ* **195**, L51–L53.

Hwang, U., Laming, J. M., Badenes, C. et al. (2004), *ApJ* **615**, L117–L120.

Indebetouw, R., Matsuura, M., Dwek, E. et al. (2014), *ApJ* **782**, L2.

Janka, H.-T. (2012), *Annual Review of Nuclear and Particle Science* **62**, 407–451.

Janka, H.-T. (2017), *Neutrino-Driven Explosions*, Springer International Publishing AG, p. 1095.

Janka, H.-T., Gabler, M. and Wongwathanarat, A. (2017), Spatial distribution of radionuclides in 3D models of SN 1987A and Cas A, *in* A. Marcowith, M. Renaud, G. Dubner, A. Ray and A. Bykov, eds, 'Supernova 1987A:30 years later - Cosmic Rays and Nuclei from Supernovae and their Aftermaths', Vol. 331 of *IAU Symposium*, pp. 148–156.

Janka, H.-T., Langanke, K., Marek, A., Martínez-Pinedo, G. and Müller, B. (2007), *Phys. Rep.* **442**, 38–74.

Janka, H.-T., Marek, A. and Kitaura, F.-S. (2007), Neutrino-Driven Explosions Twenty Years After SN 1987A, *in* S. Immler, K. Weiler and R. McCray, eds, 'Supernova 1987A: 20 Years After: Supernovae and Gamma-Ray Bursters', Vol. 937 of *American Institute of Physics Conference Series*, pp. 144–154.

Jansen, F., Lumb, D., Altieri, B. et al. (2001), *A&A* **365**, L1–L6.
Kamper, K. W. (1980), *The Observatory* **100**, 3–4.
Kepler, J. (1606), *De Stella nova in pede serpentarii, et qui sub ejus exortum de novo iniit, Trigono igneo*, 1 edn, Paul Sessius, Praha, Kingdom of Bohemia.
Kirsch, M. G., Briel, U. G., Burrows, D. et al. (2005), Crab: the standard x-ray candle with all (modern) x-ray satellites, *in* O. H. W. Siegmund, ed., 'UV, X-Ray, and Gamma-Ray Space Instrumentation for Astronomy XIV', Vol. 5898 of *Proc. SPIE*, pp. 22–33.
Kirshner, R. P., Sonneborn, G., Crenshaw, D. M. and Nassiopoulos, G. E. (1987), *ApJ* **320**, 602–608.
Kunkel, W., Madore, B., Shelton, I. et al. (1987), *IAU Circ.* **4316**.
Kushnir, D. and Katz, B. (2015), *ApJ* **811**, 97.
Larsson, J., Fransson, C., Östlin, G. et al. (2011), *Nature* **474**, 484–486.
Larsson, J., Fransson, C., Spyromilio, J. et al. (2016), *ApJ* **833**, 147.
Lattimer, J. M. and Prakash, M. (2001), *ApJ* **550**, 426–442.
Lentz, E. J., Bruenn, S. W., Hix, W. R. et al. (2015), *ApJ* **807**, L31.
Lopez, L. A. and Fesen, R. A. (2018), *Space Sci. Rev.* **214**, #44.
Luo, J., Ng, C.-Y., Ho, W. C. G. et al. (2015), *ApJ* **808**, 130.
Lyman, J. D., Bersier, D., James, P. A. et al. (2016), *MNRAS* **457**, 328–350.
MacFadyen, A. I. and Woosley, S. E. (1999), *ApJ* **524**, 262–289.
Madsen, K. K., Harrison, F. A., Markwardt, C. B. et al. (2015), *ApJS* **220**, 8.
Manchester, R. N., Hobbs, G. B., Teoh, A. and Hobbs, M. (2005), *AJ* **129**, 1993–2006.
Marek, A. and Janka, H.-T. (2009), *ApJ* **694**, 664–696.
Matsuura, M., Dwek, E., Barlow, M. J. et al. (2015), *ApJ* **800**, 50.
Matsuura, M., Dwek, E., Meixner, M. et al. (2011), *Science* **333**, 1258.
Matz, S. M., Share, G. H., Leising, M. D., Chupp, E. L. and Vestrand, W. T. (1988), *Nature* **331**, 416–418.
McCray, R. (1993), *ARA&A* **31**, 175–216.
McCray, R. and Fransson, C. (2016), *ARA&A* **54**, 19–52.
McKee, C. F. and Ostriker, J. P. (1977), *ApJ* **218**, 148–169.
Meegan, C., Lichti, G., Bhat, P. N. et al. (2009), *ApJ* **702**, 791–804.
Meier, D. L., Epstein, R. I., Arnett, W. D. and Schramm, D. N. (1976), *ApJ* **204**, 869–878.
Melson, T., Janka, H.-T., Bollig, R. et al. (2015), *ApJ* **808**, L42.
Menon, A. and Heger, A. (2017), *MNRAS* **469**, 4649–4664.
Menon, A., Utrobin, V. and Heger, A. (2019), *MNRAS* **482**, 438–452.
Mezzacappa, A., Liebendörfer, M., Messer, O. E. et al. (2001), *Physical Review Letters* **86**, 1935–1938.
Milisavljevic, D. and Fesen, R. A. (2015), *Science* **347**, 526–530.
Mitsuda, K., Bautz, M., Inoue, H. et al. (2007), *PASJ* **59**, 1–7.
Morris, T. and Podsiadlowski, P. (2007), *Science* **315**, 1103.
Morris, T. and Podsiadlowski, P. (2009), *MNRAS* **399**, 515–538.
Müller, B. (2016), *PASA* **33**, e048.
Müller, B. and Janka, H.-T. (2015), *MNRAS* **448**, 2141–2174.
Müller, B., Melson, T., Heger, A. and Janka, H.-T. (2017), *MNRAS* **472**, 491–513.
Müller, B., Viallet, M., Heger, A. and Janka, H.-T. (2016), *ApJ* **833**, 124.
Newton, I. (1687), *Philosophiae Naturalis Principia Mathematica. Auctore Js. Newton*, 1 edn, Swem Library: Jussu Societatis Regiae ac Typis Josephi Streater, London.
Nolan, C. (2014), 'Interstellar', Movie, Paramount Pictures, Warner Bros., and Legendary Pictures.
Nordhaus, J., Burrows, A., Almgren, A. and Bell, J. (2010), *ApJ* **720**, 694–703.
Ostriker, J. P. and Gunn, J. E. (1971), *ApJ* **164**, L95.
Özel, F. and Freire, P. (2016), *ARA&A* **54**, 401–440.

Page, D., Lattimer, J. M., Prakash, M. and Steiner, A. W. (2009), *ApJ* **707**, 1131–1140.
Pavlov, G. G., Zavlin, V. E., Aschenbach, B., Trümper, J. and Sanwal, D. (2000), *ApJ* **531**, L53–L56.
Perley, R. A., Chandler, C. J., Butler, B. J. and Wrobel, J. M. (2011), *ApJ* **739**, L1.
Perna, R., Viganò, D., Pons, J. A. and Rea, N. (2013), *MNRAS* **434**, 2362–2372.
Phinney, E. S. (1989), Manifestations of a Massive Black Hole in the Galactic Center, *in* M. Morris, ed., 'The Center of the Galaxy', Vol. 136 of *IAU Symposium*, Springer Netherlands, p. 543.
Pilbratt, G. L., Riedinger, J. R., Passvogel, T. et al. (2010), *A&A* **518**, L1.
Pinto, P. A. and Woosley, S. E. (1988), *Nature* **333**, 534–537.
Prialnik, D. (2000), *An Introduction to the Theory of Stellar Structure and Evolution*, Cambridge University Press, New York City, NY.
Radhakrishnan, V. and Srinivasan, G. (1982), *Current Science* **51**, 1096–1099.
Rea, N., Borghese, A., Esposito, P. et al. (2016), *ApJ* **828**, L13.
Rees, M. J. (1988), *Nature* **333**, 523–528.
Reynolds, T. M., Fraser, M. and Gilmore, G. (2015), *MNRAS* **453**, 2885–2900.
Roques, J. P., Schanne, S., von Kienlin, A. et al. (2003), *A&A* **411**, L91–L100.
Rybicki, G. B. and Lightman, A. P. (1979), *Radiative processes in astrophysics*, New York, Wiley-Interscience.
Ryle, M. and Hewish, A. (1960), *MNRAS* **120**, 220.
Scheck, L., Janka, H.-T., Foglizzo, T. and Kifonidis, K. (2008), *A&A* **477**, 931–952.
Scheck, L., Kifonidis, K., Janka, H.-T. and Müller, E. (2006), *A&A* **457**, 963–986.
Shapiro, S. L. and Teukolsky, S. A. (1983), *Black holes, white dwarfs, and neutron stars: The physics of compact objects*, Wiley-Interscience.
Shternin, P. S. and Yakovlev, D. G. (2008), *Astronomy Letters* **34**, 675–685.
Smartt, S. J. (2009), *ARA&A* **47**, 63–106.
Soker, N. (2010), *MNRAS* **401**, 2793–2798.
Soker, N. (2017*a*), A minority view on the majority: A personal meeting summary on the explosion mechanism of supernovae, *in* A. Marcowith, M. Renaud, G. Dubner, A. Ray and A. Bykov, eds, 'Supernova 1987A:30 years later - Cosmic Rays and Nuclei from Supernovae and their Aftermaths', Vol. 331 of *IAU Symposium*, pp. 131–140.
Soker, N. (2017*b*), *Research in Astronomy and Astrophysics* **17**, 113.
Spitkovsky, A. (2006), *ApJ* **648**, L51–L54.
Sukhbold, T., Ertl, T., Woosley, S. E., Brown, J. M. and Janka, H.-T. (2016), *ApJ* **821**, 38.
Sunyaev, R., Kaniovsky, A., Efremov, V. et al. (1987), *Nature* **330**, 227–229.
Taddia, F., Sollerman, J., Fremling, C. et al. (2016), *A&A* **588**, A5.
Takahashi, T., Kokubun, M., Mitsuda, K. et al. (2016), The ASTRO-H (Hitomi) x-ray astronomy satellite, *in* 'Space Telescopes and Instrumentation 2016: Ultraviolet to Gamma Ray', Vol. 9905 of *Proc. SPIE*, p. 99050U.
Takiwaki, T., Kotake, K. and Suwa, Y. (2014), *ApJ* **786**, 83.
Tamborra, I., Hanke, F., Janka, H.-T. et al. (2014), *ApJ* **792**, 96.
Tananbaum, H. (1999), *IAU Circ.* **7246**.
Tashiro, M., Maejima, H., Toda, K. et al. (2018), Concept of the X-ray Astronomy Recovery Mission, *in* 'Space Telescopes and Instrumentation 2018: Ultraviolet to Gamma Ray', Vol. 10699 of *Society of Photo-Optical Instrumentation Engineers (SPIE) Conference Series*, p. 1069922.
Taylor, J. H. and Weisberg, J. M. (1989), *ApJ* **345**, 434–450.
Thompson, A. R., Clark, B. G., Wade, C. M. and Napier, P. J. (1980), *ApJS* **44**, 151–167.
Trundle, C., Dufton, P. L., Hunter, I. et al. (2007), *A&A* **471**, 625–643.
Vedrenne, G., Roques, J.-P., Schönfelder, V. et al. (2003), *A&A* **411**, L63–L70.
Vink, J. (2012), *A&ARv* **20**, 49.
Walborn, N. R., Lasker, B. M., Laidler, V. G. and Chu, Y.-H. (1987), *ApJ* **321**, L41–L44.

Wang, L., Wheeler, J. C., Höflich, P. et al. (2002), *ApJ* **579**, 671–677.
Weisskopf, M. C., Brinkman, B., Canizares, C. et al. (2002), *PASP* **114**, 1–24.
Weisskopf, M. C., Tananbaum, H. D., Van Speybroeck, L. P. and O'Dell, S. L. (2000), Chandra X-ray Observatory (CXO): overview, *in* J. E. Truemper and B. Aschenbach, eds, 'X-Ray Optics, Instruments, and Missions III', Vol. 4012 of *Proc. SPIE*, pp. 2–16.
West, R. M., Lauberts, A., Schuster, H.-E. and Jorgensen, H. E. (1987), *A&A* **177**, L1–L3.
White, G. L. and Malin, D. F. (1987), *Nature* **327**, 36–38.
Winkler, C., Courvoisier, T. J.-L., Di Cocco, G. et al. (2003), *A&A* **411**, L1–L6.
Wongwathanarat, A., Janka, H.-T. and Müller, E. (2010), *ApJ* **725**, L106–L110.
Wongwathanarat, A., Janka, H.-T., Müller, E., Pllumbi, E. and Wanajo, S. (2017), *ApJ* **842**, 13.
Wongwathanarat, A., Müller, E. and Janka, H.-T. (2015), *A&A* **577**, A48.
Woosley, S. E., Heger, A. and Weaver, T. A. (2002), *Reviews of Modern Physics* **74**, 1015–1071.
Wootten, A. and Thompson, A. R. (2009), *IEEE Proceedings* **97**, 1463–1471.
Zhang, W., Woosley, S. E. and Heger, A. (2008), *ApJ* **679**, 639–654.